

Linear Polarization in a Black Hole, 4U 1957+115 and its X-ray Spectral Analysis

LEV TITARCHUK,¹ ELENA SEIFINA,² PAOLO SOFFIHTTA,¹ AND DIANA MAKHINYA³

¹INAF-IAPS Via Fosso Del Cavaliere 100, 00133, Rome, Italy

²Lomonosov Moscow State University/Sternberg Astronomical Institute, Universitetsky Prospect 13, Moscow, 119992, Russia

³Lomonosov Moscow State University, branch “MSU Sarov”, Parkovaya st. 8, Sarov, Nizhniy Novgorod Region, Russia

ABSTRACT

We present a new spectro-polarimetric method for estimation of the inclination of X-ray binaries using the linear polarization (LP) value in black hole (BH) sources, based on the early paper by Sunyaev & Titarchuk (1985, ST85). The X-ray LP arises from multiple scattering of initially soft photons in a hot, optically thick Compton cloud (CC) using a flat geometry. ST85 showed that the LP degree P depends on the binary inclination i and remains independent of the photon energy. Moreover, the P follows a characteristic angular distribution based on the CC optical depth τ_0 , in particular for $\tau_0 > 10$ the LP follows the Chandrasekhar (1950) distribution. In light of the vast number of recent IXPE spectro-polarimetric observations of BHs, testing this approach in combination with spectral analysis of these sources by other missions is desirable. In particular, the BH source, 4U 1957+115 was observed with IXPE in the high/soft state for which $P \sim 2\%$ was found (Marra et al. 2024). To apply the new method, in addition to knowing P for a given source, it is necessary to estimate the CC optical depth τ_0 and then to calculate of the best-fit photon index Γ and the plasma temperature kT_e . We present the X-ray spectral analysis of 4U 1957+11 using data from *IXPE*, *NuSTAR*, *NICER*, *RXTE*, *Swift*, *Suzaku* and *ASCA*. We show that the X-ray source spectra are well described by the Comptonization model with Γ varying from 1.5 to 3. We find a monotonic increase in Γ with the mass accretion rate, \dot{M} , and a final saturation of the index at $\Gamma \sim 3$ for high \dot{M} . We determine a BH mass by the scaling method: $M_{1957} = 4.8 \pm 1.8 M_{\odot}$, assuming a source distance of 22 kpc, using H 1743–322, 4U 1630–47, and GRS 1915+105 as reference sources.

Keywords: Accretion (14) — Polarimetry (1278) — High Energy astrophysics (739) — X-ray astronomy (1810) — Stellar mass black holes (1611)

1. INTRODUCTION

One of the important issues of astrophysics is an estimation of the masses of compact objects (COs) – black holes (BHs), neutron stars, white dwarfs, since for them the mass is one of the most important available characteristics. In addition, to estimate the CO mass we need to know an orientation of such a binary in space, that is, the inclination i of the binary relative to an Earth observer. However, this information is often missing due to the remoteness of the object to estimate the parameters of a binary system (Karttunen et al. 2017). It is known that the polarization of the radiation of the accretion disk surrounding the CO carries information about the inclination i (Sunyaev & Titarchuk 1985, hereafter ST85). In connection with the recent launch of the Imaging X-ray Polarimetry Explorer (IXPE) obser-

vatory, it became possible to measure the polarization degree of the radiation from black hole X-ray binaries (BHXRBs), which provides an alternative way to estimate the inclination i .

We consider the problem of the X-ray spectral formation in the COs, in particularly a BH, because of exact measurement of the linear polarization (LP) in these objects. In the presented paper we remind a reader ideas and details of the quite old ST85 paper where the authors studied, in details, the LP value P using the plane Compton cloud (CC) geometry for a wide range of the Thomson optical depth τ_0 from 0.1 to more than 10. It is remarkable that for τ_0 (half of the slab) more than 10 they obtained a value of P which follows the classical Chandrasekhar distribution versus the inclination i (Chandrasekhar 1950) see, for example, the case

$\tau_0 = \infty$ in Figure 1. It is well known that the form of observed X-ray spectra agrees with the analytically derived Comptonization spectra (see Sunyaev & Titarchuk 1980; Titarchuk 1994, hereafter ST80 and T94, correspondingly). Here, we interpret the X-ray data for a BH in 4U 1957+115 and discuss the LP established in this source [Kushwaha et al. (2023b), Marra et al. (2024), hereafter M24].

It is well known that BHXRBS undergo a change in different spectral states (McClintock & Remillard 2006): from a low-luminosity hard state (LHS) through an intermediate state (IS) to a high-luminosity soft state (HSS). These BHXRBS demonstrate the following components in their spectra: a thermal component in the soft X-ray and a Comptonization component in the hard X-rays. The thermal component is possibly formed in the accretion disk (AD), which is interpreted as geometrically thin disk of gas like the Shakura-Sunyaev (SS) disk (see in Shakura & Sunyaev 1973). While the Comptonized component is formed in the CC and a hot CC plasma scatters photons from the accretion disk to higher energies, creating this hard X-ray emission seen in BHXRBS (see e.g. T94).

In the HSS, the AD black body dominates in the emergent spectrum (see e.g. the X-ray spectral evolution of XTE J1650–500 in Montanari et al. 2009). The polarization data give an independent constraint on the X-ray emitting region. Therefore we applied a new independent way to check how accretion processes can be disclosed using the polarization data. The IXPE instrument (Weisskopf et al. 2022) allows us to measure X-ray polarization in a wide range of stellar BHXRBS (see e.g. Saade et al. 2024).

BHXRBS are excellent laboratories for testing astrophysical models of X-ray spectral formation. A particular interest is a BHXRBS with a high luminosity in the soft X-ray range. It is often difficult to diagnose the nature and parameters of the components of the binary system, since classical methods based on the orbital and/or eclipsing variability of the source, such as the dynamical method (Karttunen et al. 2017) and the eclipse method (Tsevevich 1973), are not applicable. A striking example of such a BHXRBS is the source 4U 1957+115, discovered back in 1973 (Giacconi et al. 1974). Five years later, Margon et al. (1978) found its optical counterpart V 1408 Aql, which was identified as a binary system with an orbital period of 9.329 ± 0.011 h (Thorstensen 1987; Bayless et al. 2011). One component of the system is apparently an evolved K2 or G2V secondary star (Hakala et al. 2014), while the nature of the second component, which is assumed to be a X-ray source, is still unclear. Diagnostics of the na-

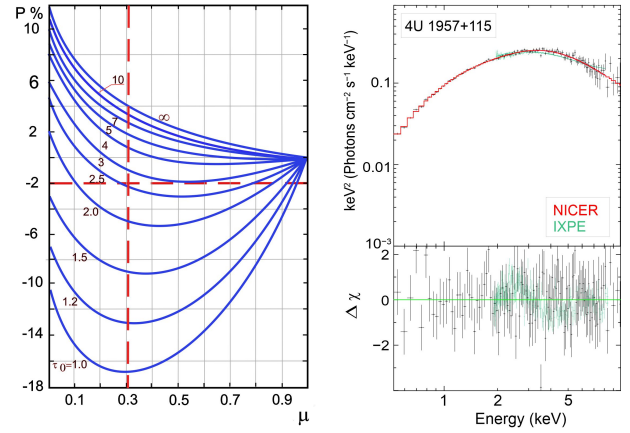


Figure 1. Left: Hard-radiation polarization degree versus $\mu = \cos(i)$ for different τ_0 (Figure is taken from ST85). The values of τ_0 are given next to the curves $P(\mu)$. Right: the X-ray spectrum of 4U 1957+115 observed by NICER (ID=610040101, red), which is simultaneous one with the IXPE observation of 4U 1957+115 (ID=02006601, green). Best-fit parameters are about $\alpha = 1$ (or the photon index $\Gamma = \alpha + 1 = 2$) and $kT_e > 10$ keV.

ture of this second component (presumably, CO) based on its mass, associated with measuring the mass function of 4U 1957+115, is very difficult because the object never enters a quiescent state (see an example of a typical X-ray light curve for 4U 1957+115 in Fig. 2). Type I bursts, which would immediately indicate a neutron star (NS) as a CO, were not registered in 4U 1957+115.

Therefore, other indirect methods for diagnosing the nature of the CO in 4U 1957+115 were used. Thus, Russell et al. (2010) used the relationship between the optical and X-ray radiation of the source and classified 4U 1957+115 as a low-mass BHXRBS. Based on the color diagrams, the source 4U 1957+115 was classified as a BH candidate in its soft spectral state (Schulz et al. 1989; White & Marshall 1984) with dominance of the accretion disk radiation and very weak X-ray variability, which has persisted over the past 48 years (Wijnands et al. 2002). The long-term X-ray flux variations in 4U 1957+115 with a period of 117 days was interpreted by Nowak & Wilms (1999) as a precessional period of an edge-on accretion disk around a compact object (BH or NS, see also Yaqoob et al. 1993; Wijnands et al. 2002). Another interpretation of this long-term X-ray variability is related to variations in the mass accretion rate through the disk due to instability caused by viscosity when the disk is irradiated by X-rays from its inner region (Wijnands et al. 2002; Ogilvie & Dubus 2001).

It is interesting that modeling of X-ray emission of 4U 1957+115 applied different models leads to significantly different results in the interpretation of the nature of this source. For an example Singh et al. (1994) and

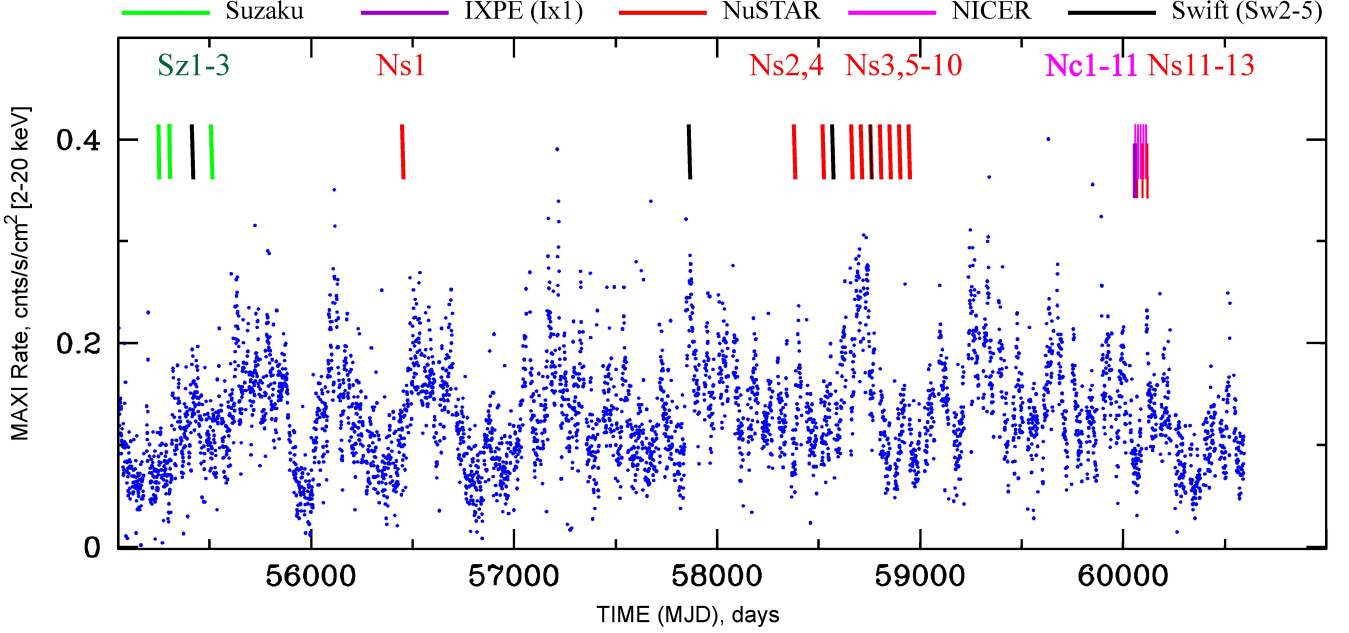


Figure 2. Evolution of X-ray from 4U 1957+115 during 2009–2024 observations with *MAXI* (2–20 keV). Red vertical lines (at top of the panel) indicate temporal distribution of the *NuSTAR* observations used in our analysis, whereas *Suzaku*, *NICER*, *IXPE*, and *Swift* observations, listed in Table 1, are indicated by green, pink, purple, and black lines.

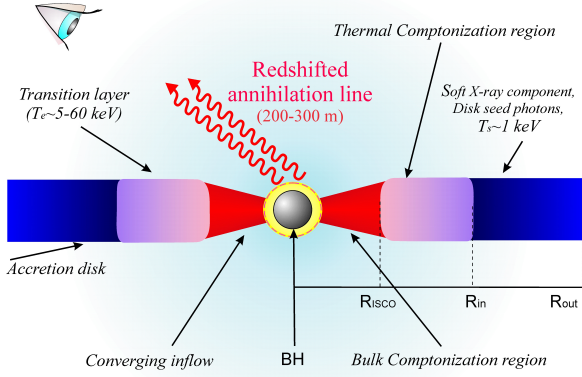


Figure 3. A suggested geometry for 4U 1957+115. Disk soft photons are up-scattered (Comptonized) off relatively hot plasma of the transition layer. In addition, we consider the region near the BH horizon where photon-photon interactions lead to the pair production effect. In this process, the created positrons interact with the accreting electrons there, and therefore annihilation line photons are created and distributed over a relatively narrow shell (marked in yellow and shown enlarged in this plot) near the BH horizon. An Earth observer should see this annihilation line only at gravitational redshift energies of $z \gg 1$.

Ricci et al. (1995) used the Comptonization model to describe the X-ray continuum using EXOSAT data and concluded that there is a BH in 4U 1957+115. Singh et al. (1994) traced an evolution of the Comptonization parameters and indicated that the plasma tem-

perature, T_e varies significantly from 12.5 keV (high-intensity state) to 1.3 keV (low-intensity one), although the optical depth varies from 4.5 (high-intensity state) to 22 (low-intensity state). At the same time, Singh et al. (1994) did not exclude a presence of a weakly magnetized NS. Yaqoob et al. (1993) applied an additive model (consisting of *bbbody* with a disk temperature $T_{in} \sim 1.5$ keV and power-law components) to analyze the spectra of 4U 1957+115 obtained during *GINGA* observations, which also indicated that 4U 1957+115 was a low-mass BHXR. It is worth noting, however that all these results strongly depend on an assumed distance to the source d and an inclination i of the object, which are strictly speaking not known. According to various estimates, d varies from 7 kpc (Sharma et al. 2021) to 20–40 kpc (Nowak et al. 2008; Gomez et al. 2015). Monte Carlo simulations of simultaneous optical and near-IR photometry of 4U 1957+115 allowed to make constraints on the distance d to be imposed from 14 kpc to 80 kpc (Hakala et al. 2014).

Some researchers reported extreme values of the inclination $i = 78^\circ$ (Maitra et al. 2014) assuming a distance of 5–10 kpc based on simulations of Swift/XRT observations. On the other hand, Gomez et al. (2015) reported an inclination angle i of 13° in a model of the source consisting of a BH with a mass of $3 M_\odot$ and a normal star companion with a mass of $1 M_\odot$, assuming orbital modulation caused by variable irradiation of the companion star’s surface during its orbital motion (Thorstensen 1987; Bayless et al. 2011). Spectral

analysis of *Chandra*, *RXTE*, and *XMM-Newton* observations of 4U 1957+115 within the relativistic accretion disk model showed that this source contained either a $3 M_\odot$ BH at a distance of 10 kpc or a $16 M_\odot$ BH at a distance of 22 kpc (Nowak et al. 2008, 2012).

Therefore, additional criteria and new observations are needed to shed light on the nature of 4U 1957+115. Analysis of *RXTE* and *ASCA* observations of 4U 1957+115 by Nowak & Wilms (1999) pointed out a NS, instead of a BH. However, the detection of a hard tail and weak variability during high luminosity states (Bayless et al. 2011; Wijnands et al. 2002; Yaqoob et al. 1993) can speak in favor of both a BH and a NS. Barillier et al. (2023) modeled the emission of 4U 1957+115 using the model *eqpair* (Coppi 1992) or the Comptonization model *thcomp* (Zdziarski et al. 2020) in combination with *polykerrbb* (Parker et al. 2019) based on *NuSTAR* and *NICER* data. They suggest a BH with a mass of $4.6 M_\odot$ at a source distance 7.8 kpc (Gaia Collaboration Brown 2021, 2016). In addition, they found a hard tail that exhibits a bidirectional behavior in normalization vs Comptonization parameter, Y diagram (see Fig. 8 in Barillier et al. 2023): two tracks, both showing a hard tail increasing with X-ray flux, but one of them has significantly stronger tails.

Regarding a peculiarity of the X-ray spectrum of 4U 1957+115, the iron emission line at 6.5 keV is only occasionally present, but is often completely absent (Nowak et al. 2008). The spectrum is also subject to interstellar absorption, $N_H = (1 - 2) \times 10^{21} \text{ cm}^{-2}$ (Nowak et al. 2008).

Recently, M24 (see also Kushwaha et al. 2023b) detected polarization of X-ray emission from 4U 1957+115 using IXPE observations. Namely, the LP degree for the source was $1.9\% \pm 0.6\%$ and polarization angle (PA) was $-41^\circ.8 \pm 7^\circ.9$ in the energy range of 2–8 keV. Spectral analysis of X-ray emission of 4U 1957+115 based on simultaneous observation by *NICER* (0.3–12 keV) and *IXPE* (2–8 keV) showed that the source was on average in the IS–HSS phase with a characteristic spectrum shape with a power-law spectral index of 1.93 ± 0.21 (M24). However, the source emission was somewhat variable (Fig. 1 in M24). This variability was clearly traced, for example, by the spectral hardness coefficient HR (Fig. 2 in M24). Namely, $HR \equiv \frac{4-12 \text{ keV}}{0.3-4 \text{ keV}}$ according to *NICER* data varied from 0.05 to 0.06, and $HR \equiv \frac{5-8 \text{ keV}}{2-5 \text{ keV}}$ varied from 0.03 to 0.05 in *IXPE* data. At the same time, *IXPE* observations, indicate that the PA in 4U 1957+115 is independent of energy. Here we used a new independent way of analyzing mass accretion processes using X-ray polarization data to take a closer look at 4U 1957+115 in this state.

In Section 2 we provide a reader details of the polarization formation of the hard X-ray emission in the plane CC around a BH. We use the polarization properties of 4U 1957+115 to derive the main parameters of this BH. Sections 3 – 4 provide the details of our data analysis and present a description of the spectral models used for fitting these data and results; Section 5 discusses the main results of the paper. In Section 6 we present our conclusions.

2. THE POLARIZATION PROBLEM FOR X-RAY PHOTONS

2.1. The linear polarization of X-ray photons in the plane Compton Cloud

We assume that the primary source of photons is distributed over the CC slab at any law, either in the central plane of the CC slab, or consists of uniformly distributed sources in the CC slab, or at the boundary of the CC.

As ST85 demonstrated the final result for photons, which undergo a number of scatterings $N \gg \tau_0^2$ much more than average for a given optical depth of the CC slab, $2\tau_0$ (see Fig. 1 in ST85) is independent of these types of the primary photon distribution.

Up-scattering (Comptonization) of low-frequency (soft) photons of $h\nu \ll kT_e$ leads to energy gain up to photon energies, $h\nu \leq 3kT_e$. It is a remarkable idea of ST85 that the polarization of X-ray photons should be independent of the photon energy which is confirmed by the *IXPE* observations (see the discussion on the constancy of $P(E)$ in observations below in Sect. 2.3).

In order to solve the integro–differential equation of the polarized radiation ST85 used the method of consecutive approximations. For $k \gg \tau_0$ the polarization of photons after these k –scatterings is independent of k . When $kT_e < 70$ keV and the Thomson approximation is valid the result of the ST85 calculations are correct (see also Pozdnyakov et al. 1983). We denote I_l and I_r as the radiation intensities related to the electric field oscillations normal to the disk plane (and of direction of photon propagation) and in the plane perpendicular to it, correspondingly. Changes of I_l and I_r in the CC plane have been calculated by the transport equations [Chandrasekhar (1950), see also, Titarchuk et al. (2025)]

$$\begin{aligned} \mu \frac{d}{d\tau} [I_l(\tau, \mu), I_r(\tau, \mu)] &= [I_l(\tau, \mu), I_r(\tau, \mu)] \\ &- \int_0^1 P(\mu, \mu') [I_l(\tau, \mu'), I_r(\tau, \mu')] d\mu' - [F_l(\tau), F_r(\tau)], \end{aligned} \quad (1)$$

where $d\tau = -\sigma_T N_e dz$, $\mu = \cos(i)$ and

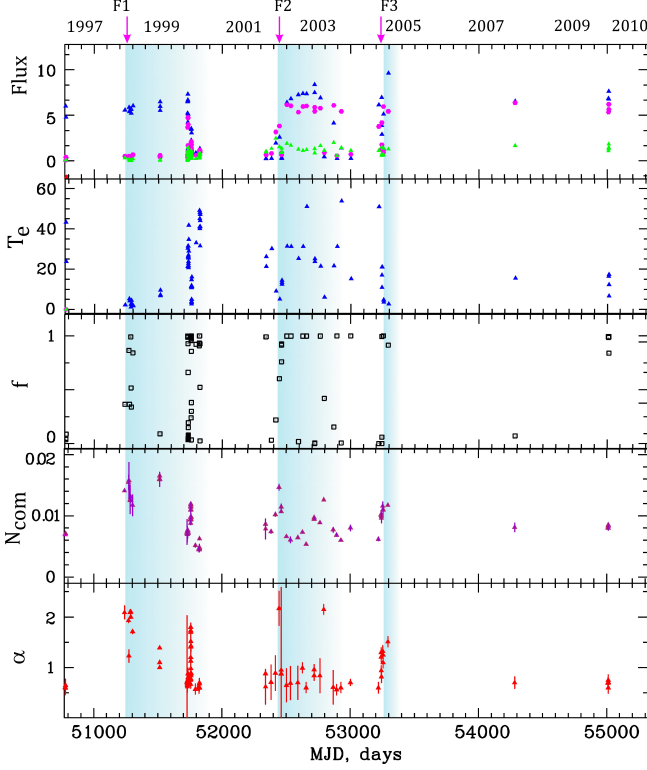


Figure 4. From top to bottom: evolution of the *RXTE* flux (in 10^{-12} erg/s/cm 2) in 3–10, 10–20 and 20–50 keV ranges (blue, crimson and green points, respectively), electron temperature T_e (in keV), Comptonized fraction f , and *CompTB* normalization N_{com} (in L_{36}/d_{10}^2) during 1997 – 2010 flare events of 4U 1957+115. In the bottom panel, we present an evolution of the spectral index $\alpha = \Gamma - 1$. The decay phases of the flares are marked with blue vertical strips. The peak outburst times are indicated by arrows at the top of the plot.

$$P(\mu, \mu') = \frac{3}{8} \begin{Bmatrix} 2(1 - \mu^2)(1 - \mu'^2) + \mu^2 \mu'^2 & \mu^2 \\ \mu'^2 & 1 \end{Bmatrix}$$

is the scattering matrix. The vector $\bar{F} = (F_l, F_r)$ specifies the distribution of primary sources.

The boundary conditions of the problem are

$$\bar{I}(\tau = 0, -\mu) = \bar{I}(\tau = 2\tau_0, \mu) = 0 \quad (2)$$

for any $0 \leq \mu \leq 1$.

The degree of the polarization is defined as:

$$P = \frac{I_r - I_l}{I_r + I_l} \quad (3)$$

and the observed intensity is a sum $I(0, \mu) = I_r(0, \mu) + I_l(0, \mu)$.

In order to find a distribution for photons which undergo k -scattering one should determine the distribution

of photons which are not scattered in the medium. In this case one should solve Eq. (1) without the scattering term but with the initial photon distribution $\bar{F}(\tau)$.

When the intensities of the first and next iterations are calculated one can proceed with the intensity of photons which undergo k -scatterings:

$$\begin{aligned} \mu \frac{d}{d\tau} [I_l^k(\tau, \mu), I_r^k(\tau, \mu)] &= [I_l^k(\tau, \mu), I_r^k(\tau, \mu)] \\ &- \int_0^1 P(\mu, \mu') [I_l^{k-1}(\tau, \mu'), I_r^{k-1}(\tau, \mu')] d\mu'. \end{aligned} \quad (4)$$

The solution of the k -iteration depending of its solution on $(k - 1)$ one (see also ST85).

In Table 2 of ST85 the authors showed that the polarization degree and angle distribution of the brightness of k -scattered are independent of the primary source distribution. To illustrate this statement the authors make their calculations for $\tau_0 = 2$ and the iteration number $N \geq 20$. The calculation results for $k \gg 1$ does not depend on k and demonstrate that these results can be applied to the polarization of the Comptonized photons (see more details in ST85, in Appendix A). It is worth to emphasize that for large optical depths ($\tau_0 \gg 5$) X-ray polarization converges to the classical solution by [Sobolev \(1949\)](#) and [Chandrasekhar \(1950\)](#).

The appropriate radiative transfer equation (1) can be rewritten in the operator form (see also §A2 in ST85). The system of equations of the polarized radiation (1) can be rewritten as

$$\bar{I} = L\bar{I} + \bar{F} \quad (5)$$

where L is the polarization integral operator. It can be checked that the operator L meets all conditions of the Hilbert-Schmidt theorem [see e.g. [Sobolev \(1966\)](#)]. Thus, L has a eigen-values \bar{p}_i and ortho-normalized eigen-functions φ_i and $p_i \rightarrow 0$ while $i \rightarrow \infty$. A vector function \bar{F} can be expanded in generalized Fourier series

$$\bar{F} = \sum_{i=1}^{\infty} a_i \bar{\varphi}_i. \quad (6)$$

Solving Eq. (5) by the method of successive approximations we find the term \bar{I}_k related to the photons underwent k -scatterings:

$$\bar{I}_k = \sum_{i=1}^{\infty} a_i p_i^k \bar{\varphi}_i. \quad (7)$$

Because of the sequence of p_i decreasing with k we obtain that

$$\bar{I}_k \simeq a_1 p_1^k \bar{\varphi}_1. \quad (8)$$

This mathematical result is illustrated by Table 2 of ST85 for $k \gg \tau_0^2$.

2.2. Determination of the main parameters of the Compton Cloud

The X-ray linear polarization P is a result of the multiple scattering of the initially soft photons in the hot CC. Multiple scattering of these soft photons leads not only to the emergent Comptonization spectrum formation but also these up-scattered X-ray photons become linearly polarized in the plane CC (see Fig. 1 in ST85).

A suggested geometry for 4U 1957+115 is presented in Fig. 3. We propose that accretion onto the BH occurs when the donor star material passes through two main zones: (i) a geometrically thin accretion disk (standard SS disk) and (ii) a transition layer (CC), where BH and disk soft photons are upscattered by hot electrons (Comptonized) by the relatively hot electrons of CC. The resulting thermal Comptonization spectrum is formed in the CC zone. In addition, we consider a zone near the BH horizon, where photon-photon interactions lead to the pair production effect. In this process, the created positrons interact with the accreting electrons there, and so annihilation line (AL) photons are created and distributed over a relatively narrow shell (marked in yellow and shown enlarged in this plot) near the BH horizon. An Earth observer can see this AL at energies much lower than those in the laboratory (~ 500 keV). Namely, only at energies taking into account the gravitational redshift $z \gg 1$ (~ 20 keV).

In this consideration the polarization degree should be independent of the photon energy for photons which undergo many scattering until they reach the 2–8 keV energy range of the IXPE (see §2 in ST80).

ST80 (see also ST85) solved the problem of the X-ray spectral formation in the bounded medium. In particular, for the slab geometry they derived a formula of the spectral index α (and $\Gamma = \alpha + 1$):

$$\alpha = -\frac{3}{2} + \sqrt{\frac{9}{4} + \gamma}, \quad (9)$$

where $\gamma = m_e c^2 \beta / kT_e$, $\beta = \pi^2 / [12(\tau_0 + 2/3)^2]$, and τ_0 is the optical depth of a half of the slab.

Using these formulas we can find the electron temperature kT_e as a function of α and β :

$$kT_e = \frac{\beta m_e c^2}{(\alpha + 3/2)^2 - 9/4}. \quad (10)$$

ST85 calculated the transfer of the polarized radiation using the iteration method. A number the iterations should be much more than average number of scatterings in a given flat CC. As a result they made a plot of the LP as a function of $\mu = \cos(i)$, where i is an inclination angle of the system for a different Thomson optical depths of $2\tau_0$. ST85 calculated the LP for τ_0 from 0.1 to 10,

and for $\tau_0 > 10$ they found that the LP follows the well known Chandrasekhar distribution (Chandrasekhar 1950).

Let us recall that for a CO (BH or NS) in 4U 1957+115 $P = 1.9 \pm 0.6\%$ (M24), which is observed in the IS–HSS. The source state was identified by modeling the spectrum with the best-fit parameter of the power-law index $\Gamma \sim 2$ (M24). Using the values of P and $i \sim 70^\circ$ (Maitra et al. 2014), we can estimate $\tau_0 \sim 2.5$ (see Fig. 1). Note that knowing the polarization, with a plot of LP against τ_0 , we can refine the inclination $i \sim 72^\circ$.

2.3. Discussion of the polarization results

It is known that observations allow us to calculate the absolute value of polarization $|P|$ (or $|LP|$), but do not determine the sign of the polarization of the X-ray source. Therefore, a sign of the observed polarization degree (see Fig. 1), for example for 4U 1957+115, and the place of the LP in LP vs τ_0 diagram can be obtained using the following arguments.

If we choose the positive values, $P > 2\%$ then we obtain that the inferred value, τ_0 for $\mu = \cos(i) = \cos(70^\circ) \approx 0.3$. But this value of $\tau_0 \sim 7$ contradicts to the observed value of the index, $\Gamma \sim 2$ (Marra et al. 2024) or the Comptonization parameter $Y \sim (kT_e/m_e c^2)(2\tau_0)^2 \propto \alpha^{-1}$. In fact, using values of $\tau_0 \sim 7$ and $kT_e > 10$ keV (see Fig. 1), the emergent spectrum should have the Wien shape ($Y > 1$), which contradicts to the X-ray observations (Marra et al. 2024). Namely, we should choose a negative polarization value of P for 4U 1957+115.

As for the refinement of the CC geometry one can choose between the spherical or the plane ones. But for the spherical one P is almost zero [compare that with that in NS case (Farinelli et al. 2024)]. It is worth noting that the linear polarization can be only if there is a strong asymmetry in the source. The negative values of the polarization P about 2% for 4U 1957+115 leads to estimates of τ_0 about 2.5 (see Fig. 5 in ST85 and Fig. 1 here).

Note also that in practice, for many BHXRBs, the polarization degree P is observed to increase with photon energy E (see e.g. Rodriguez Cavero et al. 2023; Ratheesh et al. 2024; Krawczynski et al. 2022; Kushwaha et al. 2023a,b; Rawat et al. 2023; Majumdar et al. 2023a,b; Veledina et al. 2023; Svoboda et al. 2024a,b; Steiner et al. 2024; Ingram et al. 2024; Podgorny et al. 2024; Majumdar et al. 2025). However, it should be noted that the increasing trend $P(E)$, for example, in 4U 1630–47 ranges from 6 to 12% in the energy range 2–8 keV (Table 1 in Ratheesh et al. 2024) and (Kushwaha et al. 2023b). On the other hand,

the photon indices Γ in these measurements range from 2.6 to 4.5 (Ratheesh et al. 2024; Rodriguez Caverio et al. 2023). This indicates that the polarization detection was made when the source underwent significant changes in the spectral states. It is important to emphasize that the quasi-constancy of $P(E)$ can be only ensured if the $P(E)$ distribution is determined within the same spectral state. It is also not yet clear whether this change is caused by relativistic effects near the inner edge of the disk, while the polarization of the emerging disk radiation is energy independent. This remains to be confirmed with more observations, in fact, with more sensitive polarimetry towards 10 keV and higher in future missions. But it is clear now that X-ray photons in order to be polarized they should be formed in the plane-like CC and undergoes quite a few scatterings, more than average. In this case the polarization properties of these X-ray photons depends on the geometry of the CC but not on the photon energy.

Saade et al. (2024) (hereinafter S24) compare the X-ray polarimetric properties of stellar mass BHs and supermassive BHs. In their Fig. 1 they plot the polarization degree (PD, in %) as a function of the BH inclination i . They found that the range of inclinations i for Galactic BHs is well constrained (see above), while for extragalactic BHs (EBHs) they have a very broad distribution within about 60° . However, the PD values for these EBHs are typical of those calculated in ST85 and presented here in Fig. 1. It is not by chance that S24 noted that the polarization properties for these two types of sources are similar. It is easy to see that the range of optical depths is $\tau_0 \sim 1 - 1.5$.

3. DATA SELECTION

4U 1957+115 was observed by *RXTE* (1996–2010), *Suzaku* (2010), *ASCA* (1994), *Swift* (2007–2019), *NuSTAR* (2013–2023), *IXPE* (2023) and *NICER* (2023). We extracted these data from the HEASoft (HEASARC 2014) archives and found that these data cover a wide range of X-ray luminosities. Data description see in A.1–A.7. 4U 1957+11 was also observed with MAXI (Matsuoka et al. 2009), whose light curve reproduces the quasi-continuous long-term variability of the source and helps to match pointed observations with the total flux in the 2–20 keV range (Fig. 2).

4. RESULTS

4.1. X-ray light curve

To show the distribution of *Suzaku*, *Swift*, *NuSTAR*, *IXPE* and *NICER* observations of 4U 1957+115, we have marked the times of their observations with green, black, red, purple and pink vertical lines, respec-

tively (see Fig. 2) along the MAXI light curve (2 – 20 keV). The distribution of *RXTE* observations is shown in Fig. 4.

4.2. Spectral analysis

The broadband spectrum of 4U 1957+115 was simulated within the XSPEC v12.14.1 software package using an additive model consisting of the Comptonization component CompTB (Farinelli & Titarchuk 2011) and the iron K_α emission line at 6–8 keV described by the Gaussian model. The CompTB component is applicable to any state and Comptonization type (thermal or dynamic) for the observed X-ray spectra of BHs or NSs (Titarchuk & Seifina 2024; Titarchuk et al. 2023; Titarchuk and Seifina 2023, 2021; Titarchuk et al. 2020; Titarchuk and Seifina 2017, 2016a,b; Seifina et al. 2014; Farinelli & Titarchuk 2011; Titarchuk et al. 2010; Titarchuk and Seifina 2009) and describes the continuous X-ray spectrum of the source formed as a result of Comptonization of soft “seed” photons in a CC of hot electron plasma located near the compact object. In addition, the CompTB model calculates the soft excess and the primordial emission self-consistently. In this model, see Figure 3, the total emission is determined by the CompTB normalization N_{com} , which is proportional to a mass accretion rate \dot{M} and the spectral index α (or the photon index $\Gamma = \alpha + 1$). The disk emission appears as the blackbody emission with a color temperature T_s at radii $R_{TL} < R < R_{out}$, where R_{out} and R_{TL} are the outer radius of the AD and the outer radius of the transition layer (TL), respectively. At $R < R_{TL}$, the AD emission comes out as the Comptonized emission from the warm and optically thick medium, rather than as the thermal one. The hot and optically thin TL is located in the inner part of the AD around a BH ($R < R_{TL}$), and this region forms a high-energy power-law continuum. The total Comptonized radiation is a result of the Comptonization in the X-ray energetic TL and the BH-converging inflow (*Bulk Comptonization region*), where thermal and dynamical Comptonizations are effective). A fraction of the Comptonized radiation ($f = A/(1+A)$ or $\log A$) can be found using this model fit. The seed photon temperature T_s and the TL spectral index of the corona determine the energy of the upward-scattered off soft excess radiation. The plasma temperature of accretion flow T_e (temperature of the electrons in keV) is also the parameter of the CompTB model. The Comptonization continuum can be calculated as a convolution of the soft Blackbody radiation with the Comptonization Green function G , which can be approximated as

$$G(x, x_0) = x^{-\alpha}, \quad \text{for } x > x_0,$$

$$G(x, x_0) = x^{\alpha+3}, \quad \text{for } x < x_0,$$

Table 1. Details of ASCA, *Suzaku*, *Swift*, *NuSTAR*, *IXPE* and *NICER* observations of 4U 1957+115.

Epoch	Mission	Obs. ID	Start time (UT)	Exposure (s)	MJD interval
A1	ASCA	42006000	1994 Oct 31 12:40:53	9867	49656.5–49657.2 ¹
Sz1	<i>Suzaku</i>	405057010	2010 May 4 10:00:12	31158	55320.4–55321.4 ²
Sz2	<i>Suzaku</i>	405057020	2010 May 17 12:27:24	29509	55333.5–55334.4 ²
Sz3	<i>Suzaku</i>	405057030	2010 Nov 1 19:51:40	30317	55501.8–55501.9 ²
Sw1	Swift	00030959001	2007 July 1 13:10:50	182	54282.5–4282.6 ⁵
Sw2	Swift	00091070001	2011 May 19 11:42:42	61270	55700.4–55890.5 ⁵
Sw3	Swift	00030959006	2017 Apr 27 15:30:29	925	57870.6–57870.9
Sw4	Swift	00088692001	2019 Mar 13 18:11:31	5509	58555.7–58556.6 ⁵
Sw5	Swift	00088975002	2019 May 9 01:23:27	5448	58731.–58818.1 ⁵
Ns1	<i>NuSTAR</i>	30001015002	2013 Nov 16 15:16:07	6379	56612.6–56612.7 ^{3,4,5}
Ns2	<i>NuSTAR</i>	30402011002	2018 Sep 16 20:06:09	37250	58377.3–58378.5 ^{3,4,5}
Ns3	<i>NuSTAR</i>	30502007002	2019 Apr 29 20:41:09	20730	58602.8–58603.0 ^{3,4,5}
Ns4	<i>NuSTAR</i>	30402011004	2019 Mar 13 10:01:09	10110	58555.4–58555.8 ^{3,4,5}
Ns5	<i>NuSTAR</i>	30402011006	2019 May 15 12:01:09	37020	58618.5–58619.8 ^{3,4,5}
Ns6	<i>NuSTAR</i>	30502007004	2019 June 4 19:56:09	20053	58638.8–58639.1 ^{3,4,5}
Ns7	<i>NuSTAR</i>	30502007006	2019 July 19 06:11:09	18370	58683.2–58683.4 ^{3,4,5}
Ns8	<i>NuSTAR</i>	30502007008	2019 Sep 10 01:36:09	10110	58683.2–58683.3 ^{3,4,5}
Ns9	<i>NuSTAR</i>	30502007010	2019 Oct 20 12:51:09	19640	58776.5–58776.7 ^{3,4,5}
Ns10	<i>NuSTAR</i>	30502007012	2019 Oct 30 20:56:09	20530	58817.8–58818.0 ^{3,4,5}
Ns11	<i>NuSTAR</i>	30902042002	2023 May 15 08:01:09	18680	60079.3–60079.5 ⁶
Ns12	<i>NuSTAR</i>	30902042004	2023 May 19 00:21:09	20190	60083.0–60083.2 ⁶
Ns13	<i>NuSTAR</i>	30902042006	2023 May 24 05:41:09	20570	60088.2–60088.4 ⁶
Ix1	<i>IXPE</i>	02006601	2023 May 12 02:41:23.184	571490	60076.1–60088.8 ⁷
Nc1	<i>NICER</i>	6100400101	2023 May 12 12:07:41	657	60076.54–60076.55
Nc2	<i>NICER</i>	6100400102	2023 May 14 08:39:00	2943	60078.36–60078.39
Nc3	<i>NICER</i>	6100400103	2023 May 15 01:32:40	4820	60079.06–60079.12
Nc4	<i>NICER</i>	6100400104	2023 May 16 02:19:40	8000	60080.09–60080.18
Nc5	<i>NICER</i>	6100400105	2023 May 17 00:00:00	5072	60081.00–60081.06
Nc7	<i>NICER</i>	6100400107	2023 May 19 00:29:40	4043	60083.02–60083.07
Nc8	<i>NICER</i>	6100400108	2023 May 20 01:14:20	5651	60084.05–60084.12
Nc9	<i>NICER</i>	6100400109	2023 May 20 00:14:40	8803	60085.01–60085.13
Nc10	<i>NICER</i>	6100400110	2023 May 22 01:17:00	2926	60086.05–60086.09
Nc11	<i>NICER</i>	6100400111	2023 May 23 00:22:20	4530	60087.01–60087.06

Columns 1 – 7 denote Epoch, Mission Name, Observation ID, Start time (UT), Exposure time (s), MJD interval, respectively. See the text for details. (1) Ricci et al. (1995); (2) Nowak et al. (2012); (3) Barillier et al. (2023); (4) Sharma et al. (2021); (5) Draghis et al. (2023); (6) this work; and (7) Marra et al. (2024);

where $x = hv/kT_e$, x_0 is the breakpoint of $G(x, x_0)$ where the two cases ($x > x_0$ and $x < x_0$) meet each other. Therefore, the general model consists of a Blackbody-like (BB) and a Comptonized component (XSPEC models “BMC”, “COMPTB”, “COMPTT” are the sum of these components: $BB + f \cdot BB * G$). The bulk parameter of *CompTB* model, δ , which indicates an efficiency of the bulk motion with respect to the thermal Comptonization one, for simplicity we assume as $\delta = 0$.

For 4U 1957+115 we used the Comptonization model *CompTB* modified by the additive *Gaussian* line at ~ 6.5

keV. The parameters of a *Gaussian* component are a centroid line energy E_{line} , the width of the line σ_{line} and normalization, N_{line} to fit the data in the 6 – 8 keV energy range. We also apply interstellar absorption (*tbabs* model) with column density N_H (see Table 3). The resulting model reads in XSPEC as *tbabs*(CompTB+Gaussian)*.

Different X-ray missions have observed 4U 1957+115 during different spectral states at different times, giving us an idea of what is happening to this source in X-rays.

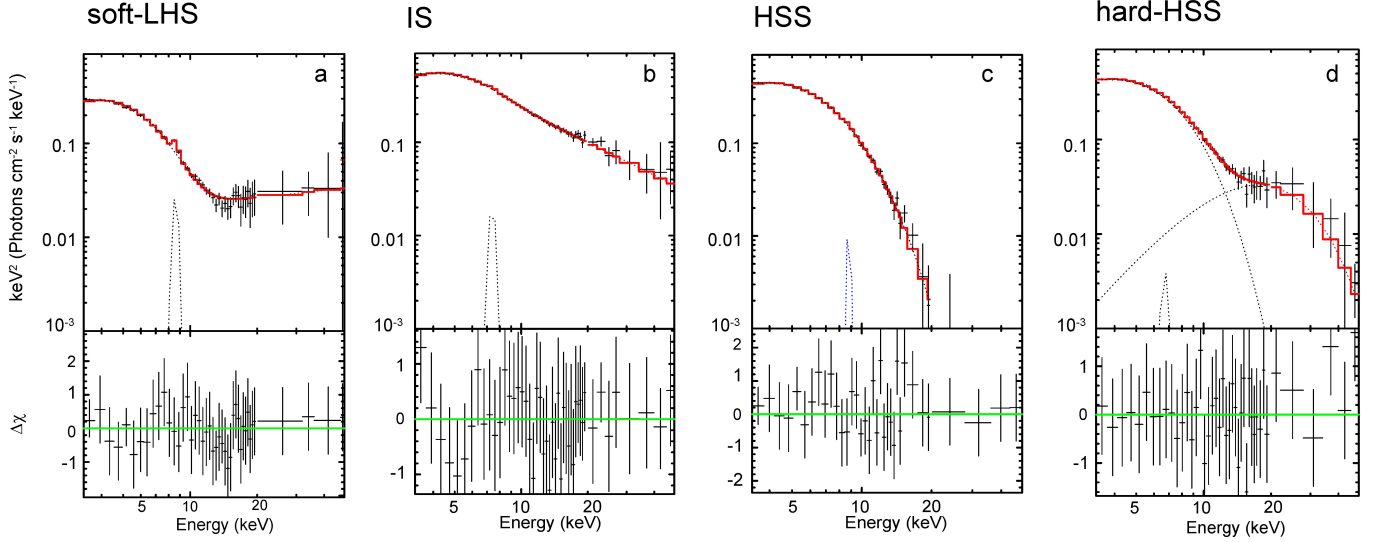


Figure 5. Representative $E * F(E)$ spectral diagrams that are related to different spectral states of 4U 1957+115 using *RXTE* observation 50128-01-05-05 (soft-LHS), 70054-01-04-00 (IS), 40044-01-03-03 (HSS), and 70054-01-01-01 (hard-HSS) with the best-fit modeling. The data are denoted by crosses, while the spectral model is shown by a red histograms for each state. Bottom: $\Delta\chi$ vs photon energy in keV.

Table 2. The list of sets of *RXTE* observation of 4U 1957+115.

Set	Dates, MJD	Obs. ID	Dates UT
R1	50778–50781	20184 ^{1,2}	Nov 26, 1997 – Nov 29, 1997
R2	51240–51514	40044 ²	Mar 3, 1999 – Dec 1, 1999
R3	51729–52927	50128, 70014, 70054	July 4, 2000 – Oct 15, 2003
R4	53242–53294	90063, 90123 ³ ,	Aug 25, 2004 – Oct 16, 2004
R5	54282.5–54282.7	93406 ²	July 1, 2007
R6	55010–55013	94311 ²	June 28, 2009 – July 1, 2009
R7	55321–55323	95335 ²	May 5, 2010 – May 7, 2010

References: (1) Nowak & Wilms (1999); (2) Wijnands et al. (2002) and (3) Nowak et al. (2008).

4.2.1. Evolution of spectral properties during different X-ray state transitions

Spectral analysis of 4U 1957+115 using observations by *ASCA*, *Suzaku*, *RXTE*, *IXPE*, *Swift*, *NICER* and *NuSTAR* indicates that the source spectra can be reproduced by a model with an absorbed Comptonization component, with an addition of *Gaussian* iron line

Table 3. Basic information on 4U 1957+115

Source parameter	Value
Mass of primary star, M_{\odot}	3–20 ^(a,b)
Class of primary star	BH ^(b) , NS ^(c)
Mass of secondary star	1 ^(a)
Class of secondary star	K2, G2V ^(d)
Inclination, i , deg	13 ^(a,d) –78 ^(e)
Distance, d , kpc	5–10 ^(e) , 10–22 ^(b) , 20–40 ^(d,e,f) 6–80 ^(g)
RA (J2000), α	19 ^h 59 ^m 24.1253 ^s ^(h)
Dec (J2000), δ	+11° 42′ 32.155″ ^(h)
Alternative names	V1408 Aql, 2SXPS J195924.1+114231 1RXS J195924.2+114235
$N_{H,Gal}$, cm^{-2}	(1–2) $\times 10^{21}$ ^(b,i)
m_V , mag	≈ 19.0 ^(d)
Parallax π , mas	0.07 \pm 0.15 ^(j)

^(a) Gomez et al. (2015); ^(b) Nowak et al. (2008); ^(c) Singh et al. (1994); ^(d) Hakala et al. (2014); ^(e) Maitra et al. (2014); ^(f) (Sharma et al. 2021); ^(g) (Gaia Collaboration Brown 2021, 2016); <https://www.swift.ac.uk/2SXPS/>; ^(h) Margon et al. (1978); ⁽ⁱ⁾ Marra et al. (2024); and ^(j) Kravtsov et al. (2022).

component. In the analyzed observations, 4U 1957+115 exhibits enhanced flare activity (see Figs. 2 and 4), accompanied by a change of its spectral shape.

4U 1957+115 smoothly evolves between different spectral states, from the LHS ($1.7 \leq \Gamma < 2$ and $20 \leq$

Table 4. Best-fit parameters of spectral analysis of some *ASCA*, *Suzaku*, *Swift*, *NuSTAR* and *NICER* observations of 4U 1957+115[†].

Epoch	$\alpha =$ $\Gamma - 1$	T_s , keV	T_e , keV	$\log(A)$	$N_{com}^{\dagger\dagger}$	E_{gauss} , keV	$N_{gauss}^{\dagger\dagger}$	$N_{htbb}^{\dagger\dagger}$	χ^2_{red} (dof)
A1	0.73±0.04	0.40±0.02	18.52±0.02	2.00 ^{†††}	6.69±0.03	7.01±0.06	0.01±0.01	0.00001(1)	1.07(277)
Sz1	0.73±0.01	0.561±0.005	28.52±0.02	2.00 ^{†††}	8.30±0.03	6.64±0.08	0.02±0.01	0.00001(1)	1.03(2492)
Sz2	0.92±0.02	0.557±0.005	29.52±0.02	2.00 ^{†††}	5.95±0.03	6.78±0.09	0.01±0.01	0.00001(1)	1.12(2297)
Sz3	0.86±0.03	0.561±0.006	21.52±0.02	2.00 ^{†††}	5.43±0.03	6.52±0.03	0.01±0.01	0.00001(1)	0.96(2244)
Sw1	2.05±0.04	1.84±0.09	7±0.2	2.00 ^{†††}	15.08±0.01	6.4±0.2	0.01±0.01	0.00001(1)	1.21(334)
Sw2	1.3±0.1	1.12±0.09	10±0.1	-0.14±0.02	10.5±0.2	6.5±0.1	0.01±0.01	0.00001(1)	1.19(933)
Sw3	1.4±0.2	1.14±0.01	11±0.1	-0.16±0.03	11.1±0.2	6.4±0.2	0.01±0.01	0.00001(1)	1.23(927)
Sw4	1.3±0.2	1.15±0.01	12±0.2	-0.12±0.01	12.98±0.06	6.4±0.1	0.01±0.01	0.00001(1)	1.02(994)
Sw5	1.4±0.1	1.17±0.03	15±0.2	-0.15±0.02	11.9±0.1	6.4±0.1	0.01±0.01	0.00001(1)	1.07(994)
Ns1	2.00±0.03	1.01±0.01	18.6±0.1	-0.76±0.01	11.25±0.02	6.95±0.03	0.02±0.01	0.0003(1)	0.99(424)
Ns2	1.95±0.04	0.98±0.02	13.1±0.2	-0.77±0.09	11.58±0.02	6.57±0.002	0.01±0.01	0.0002(1)	1.05(424)
Ns3	2.11±0.04	1.06±0.01	14.0±0.3	0.12±0.04	11.04±0.02	6.78±0.04	0.01±0.01	0.0009(1)	1.14(424)
Ns4	1.94±0.04	1.16±0.03	16.0±0.2	-0.38±0.06	12.62±0.02	6.71±0.03	0.03±0.01	0.0010(3)	1.09(424)
Ns5	2.10±0.06	1.07±0.04	15.0±0.3	-0.38±0.01	11.09±0.01	6.52±0.08	0.02±0.01	0.0007(1)	1.05(424)
Ns6	1.97±0.06	1.21±0.01	12.0±0.1	-0.42±0.01	12.42±0.02	6.95±0.07	0.01±0.01	0.001(1)	1.13(424)
Ns7	1.95±0.09	1.03±0.02	18.0±0.4	1.12±0.01	13.01±0.12	6.64±0.02	0.04±0.02	0.0034(1)	1.07(424)
Ns8	1.71±0.06	1.02±0.02	15.0±0.2	2.00 ^{†††}	14.21±0.12	6.52±0.08	0.01±0.01	0.0036(1)	1.08(549)
Ns9	1.98±0.06	1.10±0.01	18.0±0.4	-0.72±0.01	11.64±0.02	6.7±0.1	0.05±0.03	0.0004(2)	0.97(424)
Ns10	2.20±0.09	1.02±0.03	17.0±0.1	-0.71±0.01	11.89±0.01	6.7±0.2	0.03±0.01	0.0002(2)	0.97(424)
Ns11	2.20±0.07	0.97±0.01	18.0±0.5	-0.41±0.01	11.44±0.01	6.71±0.08	0.04±0.02	0.0002(2)	1.06(424)
Ns12	2.14±0.09	0.97±0.02	16.0±0.2	-0.59±0.01	11.49±0.01	6.65±0.07	0.01±0.01	0.00025(1)	1.01(424)
Ns13	1.91±0.08	1.00±0.01	16.9±0.1	-0.74±0.04	11.68±0.01	6.68±0.09	0.01±0.01	0.00025(2)	1.00(424)
Nc1	1.0±0.4	0.70±0.01	6.2±0.1	-0.28±0.03	7.68±0.04	7.1±0.2	0.01±0.01	0.00001(1)	1.14(127)

Parameter errors correspond to 1σ confidence level. [†] The spectral model is *tbabs*(CompTB + Gaussian + Bbody("HTBB"))*; ^{††} normalization parameters of *Bbody* and *CompTB* components are in units of $L_{36}/d_{10}^2 \text{ erg/s/kpc}^2$, where L_{36} is the source luminosity in units of 10^{36} erg/s ; d_{10} is the distance to the source in units of 10 kpc; T_{bb} of *Bbody* component is low variable from 4.5 keV to 5.7 keV; and *Gaussian* component is in units of $10^{-3} \times \text{total photons cm}^{-2}\text{s}^{-1}$ in line; ^{†††} when parameter $\log(A) \gg 1$, it is fixed to a value 1.0 (see comments in the text); N_H varies in the range of $(0.95 - 1.7) \times 10^{21} \text{ cm}^{-2}$ (see also Barillier et al. 2023).

$kT_e \leq 50 \text{ keV}$) at the beginning of the outburst, passing through the IS in the middle of the outburst and reaching the HSS ($2.7 < \Gamma < 2.9$ and $3 \leq kT_e \leq 15 \text{ keV}$) at the outburst maximum (Fig. 10). However, in the LHS, along with the spectra typical for this state we found a number of spectra that are somewhat different from those and appear as a positive excess of soft X-rays at energies 3–5 keV in the source spectrum. We designated such spectra “soft-LHS” and associated this excess with the increased efficiency of the accretion disk radiation. The source 4U 1957+115 in the HSS, along with the spectra typical for this state ($2.7 < \Gamma < 2.9$), showed a number of spectra that were somewhat different from those, as a positive excess of hard X-rays in the source spectrum at energies 15–50 keV. We designated such spectra “hard-HSS” and we formally approximated this hard excess by a blackbody model with a relatively

high color temperature ($kT_s \sim 4 - 5 \text{ keV}$, the so-called high-temperature blackbody (HTBB) component). We associate this excess with the effects of the matter converging onto a BH (this effect is discussed in more detail in a number of papers (Titarchuk and Seifina 2009; Seifina & Titarchuk 2010; Titarchuk and Seifina 2021), as well as in the Sect. 5). Examples of the spectra in such states are shown in Figs. 5 and 7 – 9, as well as described using 4U 1957+115 data by different missions in Sects. 4.2.2 – 4.2.8. In the best-fit spectral analysis, N_H varied weakly in the range $(0.9 - 1.7) \times 10^{21} \text{ cm}^{-2}$, which is consistent with the $(0.95 - 1.7) \times 10^{21} \text{ cm}^{-2}$ estimates from the joint *NICER*/NuSTAR analysis of the 4U 1957+115 spectra (Barillier et al. 2023) and with the Galactic extinction level $2.1 \times 10^{21} \text{ cm}^{-2}$ (Wilms et al. 2000).

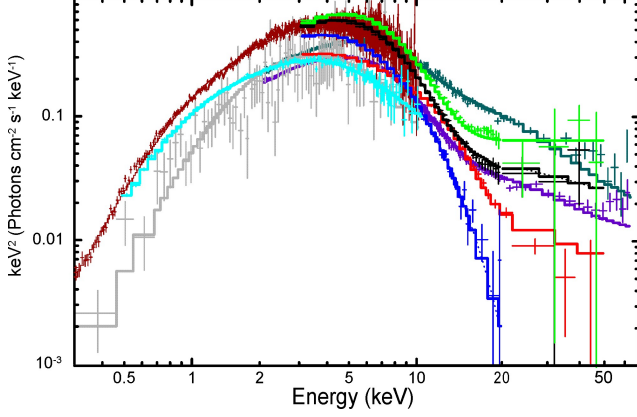


Figure 6. Representative spectra of 4U 1957+115 from *RXTE* data in units of $E * F(E)$ with the best-fit modelling for the LHS (ID=128-01-05-05, green), IS (ID=50128-01-05-02, black), hard-HSS (ID=50128-01-02-11, red) and HSS (ID=40044-01-03-03, blue) states. In addition, the *Swift* spectra of the source during the LHS (ID=00030959001, gray), and HSS (ID=00088975002, brown) states, the *NICER* spectra during the IS (ID=6100400101, bright blue) state, as well as the *NuSTAR* spectra during IS (*Ns8*, khaki) and HSS (*Ns5*, violet) are given.

Table 5. The best fit spectral parameters from IXPE observation of 4U 1957+115 for the spectro-polarimetric model $\text{tbabs}*(\text{polpow}*(\text{compTB}+\text{Gauss}))$. From left to right are, (1) model components; (2) parameters in components; (3) best fit values for Obs. Ix1. The parameters that are fixed during the fits are denoted with ^{fixed}.

Components	Parameter	Value
<i>polpow</i>	A_{norm} , %	2.77 ± 0.32
	A_{index}	-0.76 ± 0.07
	psi_{norm} , deg	-41.72 ± 0.53
	psi_{index}	0^{fixed}
<i>tbabs</i>	N_H , 10^{22} cm^{-2}	0.2 ± 0.1
<i>compTB</i>	α	1.06 ± 0.01
	kT_s , keV	0.7 ± 0.01
	kT_e , keV	6.0 ± 0.01
	$\log A$	-0.28 ± 0.03
	N_{com}^\dagger , L_{36}/d_{10}^2	7.8 ± 0.1
	E_{gauss} , keV	6.9 ± 0.1
	$N_{gauss}^{\dagger\dagger}$	4.15 ± 0.08
	χ_{red}^2 (dof)	1.32 (447)

[†] L_{36} is the source luminosity in units of 10^{36} erg/s and d_{10} is the distance to the source in units of 10 kpc. ^{††} *Gaussian* component is in units of $10^{-3} \times \text{total photons cm}^{-2}\text{s}^{-1}$ in line.

4.2.2. Spectral properties of 4U 1957+115 based on *RXTE* observations

The evolution of the spectral parameters of 4U 1957+115 in 3–60 keV range during outbursts according to *RXTE* data from 1997 to 2010 is shown in Fig. 4. The peaks of the F_1 , F_2 and F_3 outbursts are indicated by arrows in the upper part of this figure and the phases of the outburst decay are marked by vertical blue stripes. It is clearly seen that in the LHS of 4U 1957+115 the hard emission component with low Γ values, a high fraction of Comptonization f and weak X-ray normalizations N_{com} is observed.

In particular, in the *soft-LHS*, represented by the *RXTE* observation (ID=50128-01-05-05), the spectrum is dominated by a soft excess and the hard emission component (Fig. 5, panel a). This hard component is well reproduced by the Comptonization model with the following parameters: $\Gamma=1.75 \pm 0.07$, $kT_e=23.8 \pm 0.03$ keV, $N_{com}=7.67 \pm 0.01 L_{36}/d_{10}^2$ and $T_s=0.99 \pm 1$ keV (reduced $\chi^2=0.96$ for 54 d.o.f). The data are shown by black crosses and the best-fit spectral model $\text{tbabs}*(\text{CompTB}+\text{Gauss})$ by red line. In the bottom panels we show $\Delta\chi$ versus a photon energy in keV.

In the panel b (Fig. 5) we demonstrate the source spectrum (ID=70054-01-04-00) in the IS, for which the best-fit model parameters are $\Gamma=2.17 \pm 0.3$, $N_{com}=12.66 \pm 0.09 L_{36}/d_{10}^2$, $kT_e=5.1 \pm 0.09$ keV and $T_s=1.0 \pm 0.3$ keV ($\chi_{red}^2=0.98$ for 54 d.o.f).

In the HSS, the spectral parameters of the source change remarkably: soft radiation already dominates, Γ increases, the Comptonization fraction, f decreases with an increase of normalization, N_{com} . For example, in the panel c (Fig. 5), the *HSS* spectrum (ID=40044-01-03-03) is presented, where we can see the dominance of the soft emission, for which the best-fit model parameters are $\Gamma=2.10 \pm 0.3$, $N_{com}=13.7 \pm 0.4 L_{36}/d_{10}^2$, $kT_e=12.7 \pm 0.4$ keV and $T_s=0.89 \pm 0.1$ keV ($\chi_{red}^2=0.99$ for 54 d.o.f).

Finally, the panel d of Fig. 5 (*hard-HSS*) demonstrates the *HSS* source spectrum (ID=70054-01-01-01) for which the best-fit model parameters are $\Gamma=2.62 \pm 0.3$, $N_{com}=15.66 \pm 0.09 L_{36}/d_{10}^2$, $kT_e=6.25 \pm 0.06$ keV and $T_s=0.78 \pm 0.02$ keV ($\chi_{red}^2=0.95$ for 54 d.o.f).

We clearly see that the change of the spectral state from the LHS to the HSS in 4U 1957+115 is accompanied by an increase of normalization, N_{com} and an increase in the photon index Γ from 2 to 3 (red points in Figure 10). However, with a further increase in normalization (or the mass accretion rate) the photon index Γ drops from 3 to 2.4.

It is important to emphasize that in Figure 7 we show a spectral evolution from the IS to the HSS where

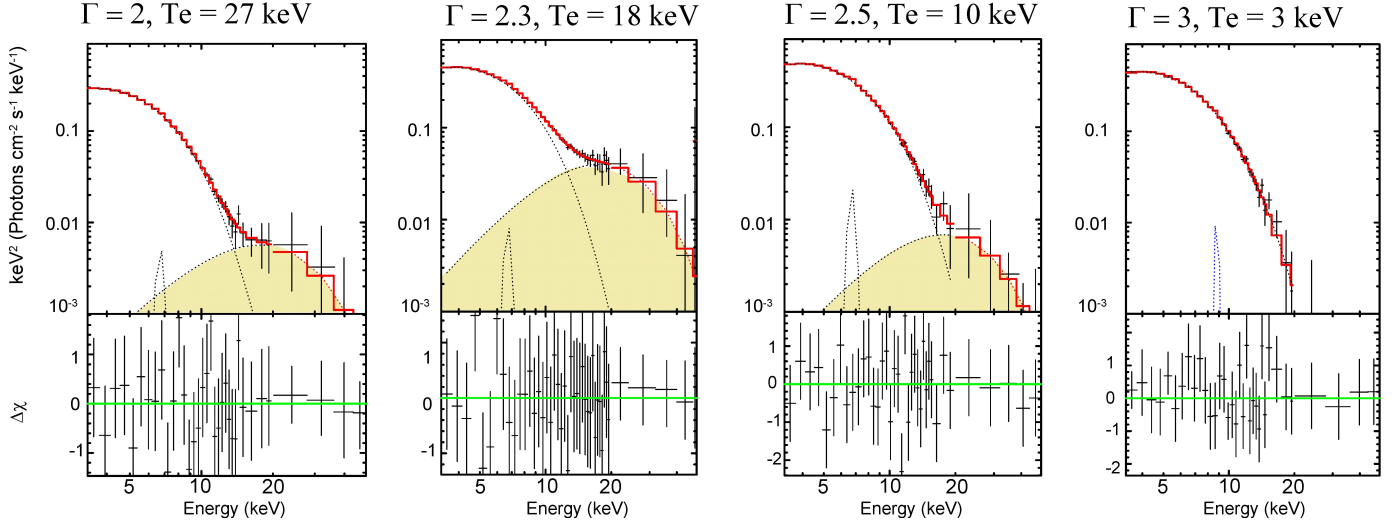


Figure 7. Representative $E * F(E)$ spectral diagrams that are related to different spectral states for 4U 1957+115 using *RXTE* observations 50128-01-03-00 ($\Gamma = 2 \pm 0.1$), 50128-01-02-11 ($\Gamma = 2.3 \pm 0.1$), 70014-05-01-04 ($\Gamma = 2.4 \pm 0.2$) and 40044-01-03-03 ($\Gamma = 3.0 \pm 0.2$). The data are shown by black points and the spectral model is displayed by red histogram. Yellow shaded areas demonstrate an evolution of the HTBB component during spectral evolution between the IS and the HSS.

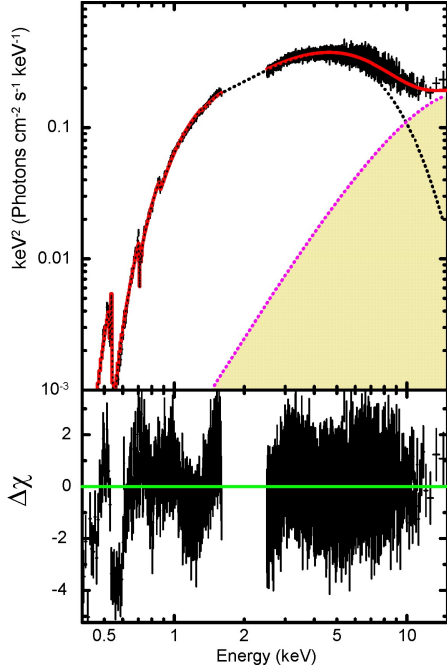


Figure 8. $E * F(E)$ spectral diagram of 4U 1957+115 using *Suzaku* data in units of $E * F(E)$ with the best-fit modeling for the HSS (ID=405057010) state. The data are shown by black points and the spectral model is displayed by red histogram. Yellow shaded areas indicates the HTBB component.

one can clear see a presence of the so-called high-temperature blackbody (HTBB) component, which appears in the IS when $\Gamma \sim 2$ and disappears in the HSS when $\Gamma \sim 3$. Below we will show that the shape of this

component can be approximated by a hot black body with a color temperature $kT_{HTBB} \sim 4 - 6$ keV.

4.2.3. Spectral properties based on *ASCA* observations

The *ASCA* observation A1 were carried out in 1994, when 4U 1957+115 was in the *soft-LHS* state. Best-fit parameters of the spectra in 0.3–10 keV range using the `tbabs*(CompTB+Gauss+Bbody)` model are $\Gamma = 1.73 \pm 0.04$, $T_e = 18.52 \pm 0.02$, $N_{com} = 6.69 \pm 0.03$, $\chi^2_{red}=1.07$ (277 dof) (yellow line in Table 4).

4.2.4. Spectral properties based on *Suzaku* observations

During the *Suzaku* observations in May – November, 2010, 4U 1957+115 was in the HSS state. The best-fit parameters of the spectra in 0.3–10 keV range using the `tbabs*(CompTB+Gauss+Bbody)` model are given in Table 4. An example of a typical observed spectrum with the best-fit model is shown in Fig. 8.

4.2.5. Spectral properties of 4U 1957+115 based on *NICER* observations

All *NICER* observations (May 12 – 23, 2023) mainly capture the 4U 1957+115 outbursts, when the object was in the IS state (Fig. 10). The best-fit parameters of the spectra in 0.5–12 keV range using the `tbabs*(CompTB+Gauss+Bbody)` model are given in Table 4. An example of a typical observed spectrum with the best-fit model is shown by red color in Fig. 1 (right panel).

4.2.6. Spectral properties of 4U 1957+115 based on *IXPE* observations

During the *IXPE* observations, 4U 1957+115 (May 12, 2023) was in the IS–HSS phase. The best-

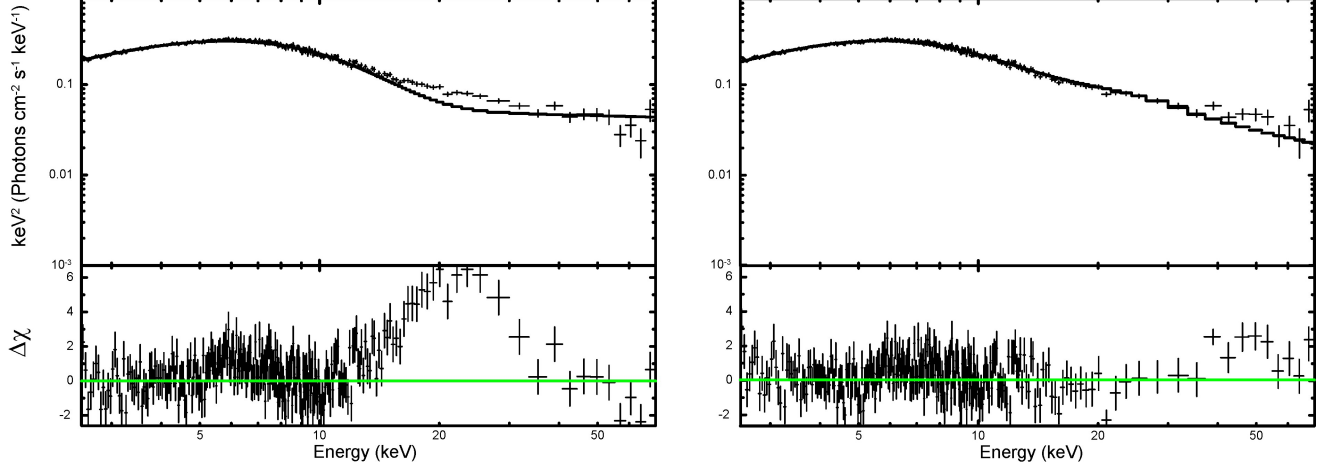


Figure 9. The best-fit spectrum of 4U 1957+115 (top) with $\Delta\chi$ (bottom) during *NuSTAR* observation *Ns8* in $E * F(E)$ units. Left: fitting without modeling the HTBB component ($\chi^2_{red} = 2.1$ for 552 dof) and right: the best-fit spectrum and $\Delta\chi$, when the bump in residuals at ~ 20 keV is modeled by a HTBB component with $\chi^2_{red} = 1.08$ for 549 d.o.f.

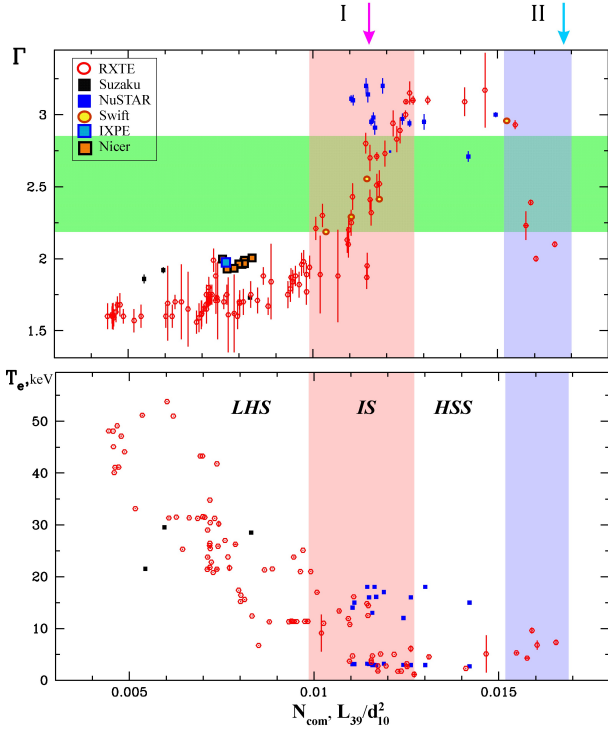


Figure 10. The photon index, Γ plotted versus the *CompTB* normalization, N_{com} (top panel) and the electron temperature T_e (in keV, bottom panel) for 4U 1957+115. Here, two zones (I and II) for $\Gamma \sim 2.2-2.8$ are also highlighted, where the appearance of the HTBB is expected (green band for Γ). The photon index, Γ decline at large *CompTB* normalizations is indicated by a vertical blue stripe (zone II). The pink vertical band (zone I) marks the normalization interval corresponding to the detection of the HTBB at average accretion rates \dot{M} ($\sim N_{com}$).

fit parameters of the spectra in 2–8 keV range using the `tbabs*(CompTB+Gauss+Bbody)` model are given in Table 5. Here we also present the results of model-dependent analysis by fitting IXPE Stokes *I*, *Q* and *U* spectra in XSPEC in frame of `tbabs*(polpow*(compTB+Gauss))` model. An observed spectrum with the best-fit model is shown by green color in Fig. 1 (right panel).

The analysis of IXPE data shows that the `polpow` model fits the observations better than, for example, `pollin` or `polconst`. On the one hand, this may indicate that polarization properties are energy dependent. And this somewhat contradicts the conclusions of ST85 that *P* does not depend on the photon energy. On the other hand, the $P(E)$ estimate for 4U 1957+115 was obtained in the time interval when the source underwent significant changes in the spectral state, MJD 60076–60088 (see Table 2 and Fig. 4 in M24). These changes are well tracked, for example, in terms of the spectral hardness coefficient *HR*, and are presented in Fig. 2 in (M24): 0.05–0.06 in NICER [$HR = (4-12\text{keV})/(0.3-4\text{keV})$] and 0.03–0.05 in IXPE [$HR = (5-8\text{keV})/(2-5\text{keV})$] observations. As already mentioned, the strict constancy of *P* with energy, according to ST85, can be ensured if the value of $P(E)$ is determined within one spectral state (e.g., HSS), without admixture of source data in other states (e.g., IS or LHS). As is known, at present the results of IXPE observations in the range of 6–8 keV suffer somewhat from poor statistics, especially for the source 4U 1957+115, which makes the presented dependence of $P(E)$ somewhat uncertain. However, IXPE observations already show that PA is independent of energy (M24, Kushwaha et al. (2023b)).

I

II

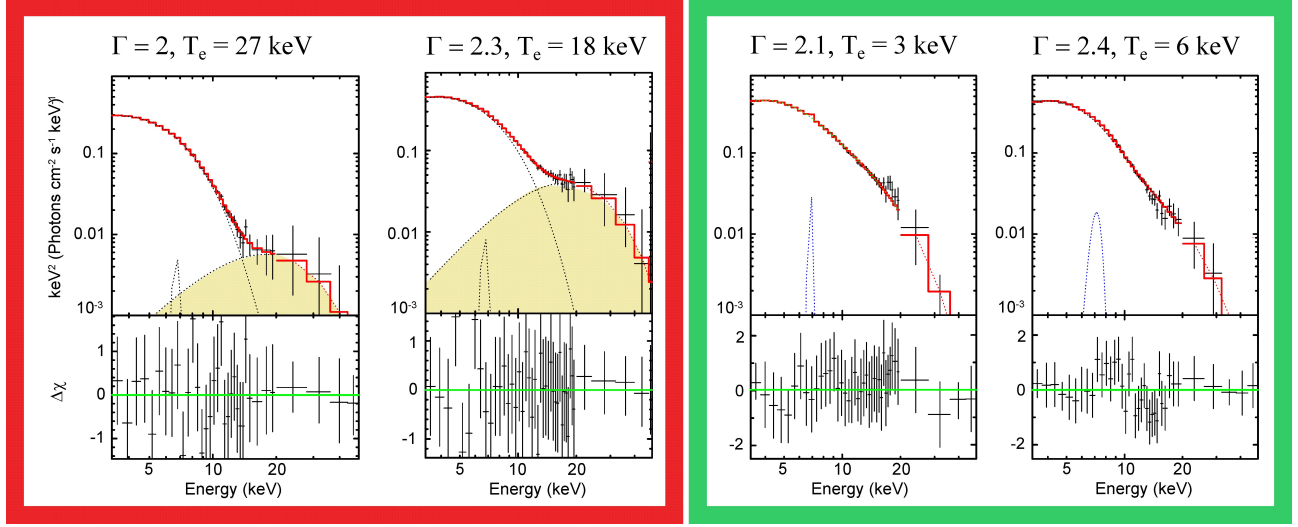


Figure 11. Difference between the spectra of 4U 1957+115 in zone I (enclosed by a red rectangle) and zone II (enclosed by a green rectangle) of the $\Gamma - N_{com}$ diagram in Fig. 10. It is evident that in zone I the contribution of the HTBB is well detected, although in zone II the spectrum is well described by the Comptonized model without any contribution of the HTBB. The best-fit spectra of 4U 1957+115 using *RXTE* observations (in zone I) 50128-01-03-00 (left) and 50128-01-02-11 (right); (in zone II) 40044-02-01-00 (left) and 40044-02-01-01 (right) are used to demonstrate this difference. The data are presented by crosses and the best-fit spectral model $tbabs*(CompTB+BB)$ by red line. Yellow shaded areas demonstrate an evolution of the HTBB component during spectral evolution between the LHS and the HSS. Bottom: $\Delta\chi$ vs photon energy in keV.

4.2.7. Spectral properties based on *Swift* observations

All *Swift* observations of 4U 1957+115 (2007 – 2019) mainly cover the time intervals with the flares, when the object underwent the spectral state transition from the IS to the HSS (Fig. 2), accompanied by a change in the spectral state (see Fig. 6). The spectral analysis of 4U 1957+115 in 0.3–10 keV range within our Comptonization model showed that the source smoothly evolves from the IS ($2.2 < \Gamma < 2.5$ and $10 \leq kT_e \leq 15$ keV; e.g., grey *S4* spectrum in Fig. 6) in the middle of the flare and reaching the HSS ($\Gamma \sim 3$ and $kT_e \sim 7$ keV; e.g., brown *S1* spectrum in Fig. 6) at the flare peak.

4.2.8. Spectral properties based on *NuSTAR* observations

NuSTAR observations cover a wide time interval from 2013 to 2023 and detect 4U 1957+115 in different spectral states from the IS to the hard-HSS. In particular, the index Γ varies around 3 (see Table 4, grey box). The typical spectra of the source in 2–60 keV range is shown in Figs. 6 (*Ns5* violet and *Ns8*, khaki) and 9. The disk seed photon temperature T_s varied weakly around 1 keV during all *NuSTAR* observations. The plasma temperature T_e is maintained at a moderate level of $T_e \sim 12 - 20$ keV, although the illumination conditions of the CC vary greatly, which is traced by variations in the parameter $\log(A)$ in a wide range, from -0.77 to 2 . Also, in the spectrum of 4U 1957+115, an iron line is detected at energies E_{gauss} from 6.5 keV to

7 keV. The normalization of the *CompTB* component is maintained at a moderate level typical for the IS–HSS phase, $N_{com} \sim (0.011 - 0.014) \times L_{39}/d_{10}^2$ (see Table 4 and Fig. 9), indicating a stable mass accretion rate \dot{M} during the *NuSTAR* observations of 4U 1957+115.

Note, that the available *NuSTAR* data allows us to study the broadband spectrum of the source (2 – 70 keV), thus, refine the model for fitting the spectrum (see Fig. 9 and discussion below in Sect. 4.3). Namely, we investigated the contribution of the HTBB component and its features taking into account its transience. We found that sometimes it reaches $0.0036 L_{36}/d_{10}^2$, and sometimes it is not detected in the spectrum at all (table 4). We fixed HTBB at the detection limit in cases where taking HTBB into account is not required when modeling the source spectrum. This approach is justified for the subsequent adequate comparative analysis of the results of fittings on different dates.

4.3. Observational evidence of the “BB-like” (HTBB) component peaked at ~ 20 keV in the IS spectra

The adopted spectral model shows a very good agreement for 47 cases out of 80 spectra of 4U 1957+115 with *RXTE* used in our analysis. A value of the reduced statistic χ^2 ($\chi_{red}^2 = \chi^2/N_{dof}$, where N_{dof} is the number of degrees of freedom for the fit, is about 1.0. for 47 observations. But for 33 of the IS observations, the fit of the data with the $tbabs*(CompTB + Gauss)$

model is not so good; χ_{red}^2 reaches 1.4 and even higher. We find that there is a characteristic bump in the data residual compared to the model at about 20 keV, which can be fitted by a BB-like shape of the color temperature at about 4.5 keV. This HTBB component is strong in each of the 33 observations (see Fig. 7).

A similar pattern can be demonstrated using NuSTAR observations of 4U 1957+115. For example, when modeling the spectrum *Ns8* with the `tbabs*(compTB + Gauss)` model, the fit is not as good, with χ_{red}^2 reaching 2.1. This spectrum is shown in the left panel of Figure 9 with the best-fit model (top) and $\Delta\chi$ (bottom). Again, as in some RXTE observations, the data residuals are found to exhibit a characteristic positive excess around 20 keV compared to the best-fit model (see the lower left panel of Figure 9). This bump is easily fitted to the BBody-like shape with the color temperature ~ 4.5 keV (see the right panel of Figure 9 and Table 4 for the best-fit parameters). Specifically, the right panel of Figure 9 (top) shows the best-fit spectrum and $\Delta\chi$ (bottom) when the bump in the residuals at ~ 20 keV is modeled by the HTBB component with $\chi_{red}^2 = 1.08$ for 549 dof, thus achieving a good statistical fit to the model.

We present the observational results in Figure 10 where the photon index, Γ plotted versus the *CompTB* normalization, N_{com} (top panel) and the electron temperature T_e (bottom panel) for 4U 1957+115. Here we marked two vertical zones that differ in the normalization N_{com} (proportional to the mass accretion rate \dot{M}): I – zone of moderate \dot{M} (pink stripe) and II – zone of high \dot{M} (blue stripe). These zones show completely different behavior of $\Gamma - N_{com}$: zone I is characterized by a monotonic increase of Γ with N_{com} , while zone II is distinguished by a decrease of Γ with N_{com} . The green horizontal stripe indicates the interval for moderate $\Gamma \sim 2.2-2.8$, where the appearance of HTBB is expected (Titarchuk and Seifina 2021). In 4U 1957+115, HTBBs are well detected in the area of intersection of the green and pink stripes, although in the area of intersection of the green and blue stripes HTBB is almost not detected.

This difference is more clear when looking at the spectra of 4U 1957+115 from these zones in detail (Figure 11). In fact, the spectra in zone I (enclosed by the red rectangle in this figure) show a well-detected HTBB contribution (HTBB is shaded in yellow), while in zone II (enclosed by the green rectangle) the spectrum is well described by the Comptonized model without any HTBB contribution (in these cases, we set the HTBB normalization to a minimum level). The key parameter here is the CC plasma temperature (see Fig. 6). So for

zone I the temperature T_e is higher (~ 20 keV) than for zone II (~ 5 keV). The reason for this behavior is discussed in Laurent & Titarchuk (2018) and Titarchuk and Seifina (2021) and the spectral shape of this feature is presumably related to the gravitational redshift, z of the AL formed near a BH horizon, where this feature is formed, and the optical depth τ of the converging flow (Laurent & Titarchuk 2018). We discuss the details of this interpretation in Sect. 5.2.

4.4. A BH mass estimate

We used a scaling technique to estimate a BH mass M_{BH} , previously developed specifically for a BH weighing [Titarchuk et al. (2025); Titarchuk & Seifina (2024); Titarchuk and Seifina (2023); Titarchuk et al. (2023); Seifina et al. (2018a,b, 2017)]. This scaling technique is widely used for a BH mass estimate. It is assumed that under outbursting conditions the characteristics of the X-ray emission from the inner region of the disk are similar for different BHs of different masses (Shaposhnikov & Titarchuk 2009, hereafter ST09), which is consistent with empirical data (Seifina et al. 2018b). The disk luminosity [see Shakura & Sunyaev (1973)] can be evaluated as:

$$L = \frac{G\dot{M}M_{BH}}{R_*}, \quad (11)$$

where G is the gravitational constant, \dot{M} is the mass accretion rate onto the BH, $R_* = r \times R_S$ is the effective radius at which the main energy release in the disk occurs, $R_S = 2G \times M_{BH}/c^2$ is the Schwarzschild radius. In the framework of this assumption, the *target* BH mass, M_t can be scaled relative to another one, *reference* BH, M_r :

$$s_N = \frac{N_r}{N_t} = \frac{m_r}{m_t} \frac{d_t^2}{d_r^2} f_G, \quad (12)$$

where N_r and N_t are normalizations of the spectra, $m_t = M_t/M_\odot$ and $m_r = M_r/M_\odot$ are the dimensionless BH masses with respect to a solar mass, and d_t and d_r are distances to the *target* and *reference* sources, correspondingly. A geometrical factor, $f_G = \cos i_r / \cos i_t$, where i_r and i_t are the disk inclinations for the *reference* and *target* sources, respectively (ST09).

We apply the $\Gamma - N$ correlation to estimate the mass of BHs (for details see ST09). This method ultimately (i) identifies a pair of BHs for which Γ correlates with an increasing normalization of N (which is proportional to a mass accretion rate \dot{M} and a BH mass M_{BH} , see Eq. (7) in ST09) and for which the saturation levels Γ_{sat} , are the same and (ii) calculates the scaling factor s_N , which allows us to determine a black hole mass of the target object.

For appropriate scaling, we need to select X-ray sources (reference sources), which also show the effect of the index saturation, namely at the same Γ level as in 4U 1957+115 (target source). For these reference sources, a BH mass, inclination, and distance must be well known. We found that GRS 1915+105, 4U 1630–47 and H 1743–322 can be used as the reference sources because these sources met all aforementioned requirements to estimate a BH mass of the target source (see items (i) and (ii) above).

In Figure 12 we demonstrate how the photon index Γ evolves with normalization N (proportional to the mass accretion rate \dot{M}) in 4U 1957+115 (*target* source) and GRS 1915+105, 4U 1630–47 and H 1743–322 (*reference* sources), where N is presented in units of L_{39}/d_{10}^2 (L_{39} is the source luminosity in units of 10^{39} erg/s and d_{10} is the distance to the source in units of 10 kpc). As we can see from this Figure that these sources have almost the same index saturation level Γ . We estimated a BH mass for 4U 1957+115 using the scaling approach (see e.g., ST09). In Figure 12 we illustrate how the scaling method works shifting one correlation versus another. From these correlations we could estimate N_t , N_r for 4U 1957+115 and for the reference sources (see Table 6). A value of $N_t = 1.02 \times 10^{-2} L_{39}/d_{10}^2$, N_r is determined in the beginning of the Γ -saturation part (see Fig. 12, ST07, ST09, Seifina et al. (2014); Titarchuk and Seifina (2016a,b, 2009)).

A value of $f_G = \cos i_r / \cos i_t$, using the *target* and *reference* sources can be obtained, using an inclination for 4U 1957+115 $i_t = 72^\circ$ and i_r (see Table 6). Thus, we obtain an estimated target BH mass, m_t (in 4U 1957+115):

$$m_t = f_G \frac{m_r d_t^2}{s_N d_r^2}, \quad (13)$$

where we used a value of $d_t = 22$ kpc (see Table 6).

As a result, we find that $M_{1957} \sim 4.8 \pm 1.8 M_\odot$ ($M_{1957} = m_t \times M_\odot$) assuming $d_{1957} = 22$ kpc for 4U 1957+115. The final error is calculated as the standard deviation relative to the mean: $\sigma(\bar{m}_t) = \sigma/\sqrt{n} = 0.45/\sqrt{3} \sim 0.27$ (see also Table 6).

Since the determination of a BH mass in 4U 1957+115 depends on a precise knowledge of the distance we plotted a BH mass versus distance for a wide range of source distances given in GAIA’s analysis (from 7 to 80 kpc, see Fig. 13). According to this plot, only starting from a source distance of 20 kpc a BH mass (m_t) in 4U 1957+115 is greater than $3 M_\odot$, i.e. indicates the presence of a black hole in 4U 1957+115. Therefore, following Nowak et al. (2008, 2012), we chose the distances $d_t = 22$ kpc, for which the calculations of the BH mass in 4U 1957+115 are presented in Table 6.

On the other hand, we found a saturation phase of the index Γ in 4U 1957+115 (Fig. 6), which, according to the spectral signatures of the BH (Titarchuk & Zannias 1998; Titarchuk and Seifina 2009, 2021), immediately indicates the presence of a BH in 4U 1957+115. Then, taking into account the graph in Fig. 8, we can impose a lower limit on the distance to the source: $d_t > 20$ kpc, which is consistent with the results of Nowak et al. (2008, 2012).

5. DISCUSSION OF THE SPECTRAL ANALYSIS

5.1. The index- \dot{M} correlations: index saturation and decrease at large \dot{M}

The source, 4U 1957+115 shows X-ray variability on time scales from weeks to months, being almost constant at a high flux level from 0.1 to 1×10^{-8} erg/s/cm² in the 3–10 keV range. Based on long-term observations of 4U 1957+115 by the *NuSTAR*, *RXTE*, *Suzaku* and *ASCA* observatories, we have found two fundamentally different types of outbursts: soft and hard, which belong to different phases (I and II) of the $\Gamma - N_{com}$ correlation.

We have classified four spectral states in this source: the softLHS, IS, HSS and hardHSS (see Fig. 5). It is shown that the spectra of the X-ray source are well described by the Comptonization model with the photon index Γ varying from 1.5 to 3. A monotonic increase in Γ with increasing accretion rate \dot{M} and saturation of Γ at the level of $\Gamma = 3$ at high values of \dot{M} during outbursts are detected. We attributed the difference in the types of outbursts to different phases in terms of the $\Gamma - N$ correlation. In addition, we discovered a unique phase of decreasing Γ from 3 to 2.4 at very high accretion rates. Such behavior is typical for a number of other X-ray binary systems with BHs (e.g., GRS 1915+105), based on which a conclusion is also made about the presence of a BH in the source. In addition, we estimated a BH mass in 4U 1957+115 by the scaling method $M_{1957} = 4.8 \pm 1.8 M_\odot$ assuming the source distance of 20 kpc, with H 1743–322, 4U 1630–47 and GRS 1915+105 as reference sources.

Finally, a significant transient feature was found in the source spectrum at energies of 10–20 keV, which we attributed to a gravitationally redshifted AL and approximated by the blackbody with a temperature of 4–5 keV. This feature is observed in the spectra of source with the photon index $\Gamma \sim 2.4$ and is presumably formed in a layer near the event horizon in 4U 1957+115. Let us discuss this interpretation in more detail below.

5.2. The HTBB in different spectral states

In Figure 10 we demonstrate the photon index, Γ , plotted against the *CompTB* normalization N_{com} (up-

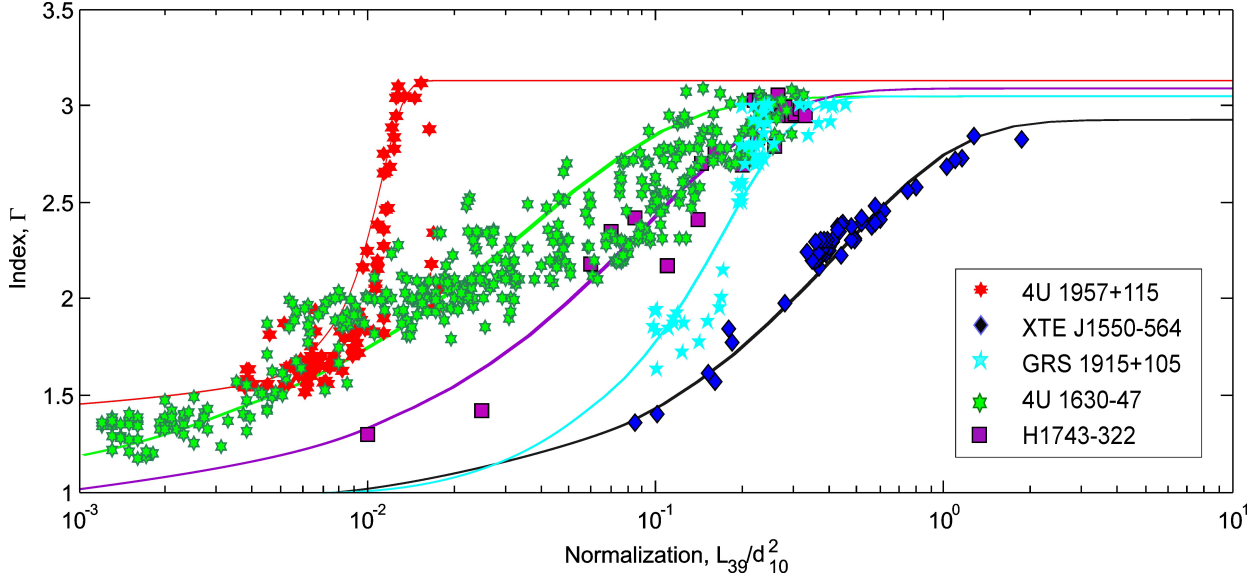


Figure 12. Scaling of photon index Γ for 4U 1957+115 (with red line for target source) with GRS 1915+105 (bright blue line), 4U 1630-47 (green line) and H 1743-322 (violet line) as reference sources).

Table 6. BH mass scaling for 4U 1957+115

Reference sources	m_r, M_\odot	$i_r^{(a)}, \text{deg}$	$N_r, L_{39}/d_{10}^2$	$d_r^{(b)}, \text{kpc}$
GRS 1915+105 ⁽²⁾	12.4 ± 2	60 ± 5	0.2 ± 0.1	9.4 ± 0.8
4U 1630-47 ⁽³⁾	10.0 ± 0.1	70	0.12 ± 0.04	10 ± 1
H 1743-322 ⁽⁴⁾	13.3 ± 3.2	70	0.19 ± 0.02	9.1 ± 1.5
Target source	m_t, M_\odot	$i_t^{(a)}, \text{deg}$	$d_t^{(b)}, \text{kpc}$	
4U 1957+115	$\sim 5.6 \times (1 \pm 0.45)$	72	$22^{(5)}$	that using GRS 1915+105 as a ref. source
4U 1957+115	$\sim 4.4 \times (1 \pm 0.45)$	72	$22^{(5)}$	that using 4U 1630-47 as a ref. source
4U 1957+115	$\sim 4.4 \times (1 \pm 0.45)$	72	$22^{(5)}$	that using H 1743-322 as a ref. source
4U 1957+115	Final estimate	72	$22^{(5)}$	as a standard deviation for a mean:
	$\sim 4.80 \times (1 \pm 0.39)$			$\sqrt{0.45/3} = 0.39$

(a) System inclination in the literature and (b) source distance found in the literature. (1) Orosz et al. (2001);

Sanchez-Fernandez et al. (1999); Sobczak et al. (1999); (2) Fender et al. (1999); Greiner et al. (2001); (3) Seifina et al. (2014); (4) McClintock et al. (2007); and (5) Nowak et al. (2008, 2012).

per panel) and the electron temperature T_e (in keV, lower panel) for 4U 1957+115. Here we also highlight two zones (I and II) for $\Gamma \sim 2.2-2.8$, where the HTBB is expected to appear (green band for Γ). The decay phase of the photon index Γ at large normalizations ($N_{com} \geq 15 \times L_{36}/d_{10}^2$) is indicated by the vertical blue band (zone II).

The pink vertical band (zone I) marks the normalization interval corresponding to the detection of the HTBB at intermediate accretion rates \dot{M} ($11 \times L_{36}/d_{10}^2 \geq N_{com} \geq 13 \times L_{36}/d_{10}^2$). It is interesting to note that similar HTBB humps was previously detected in other BH sources Cyg X-1 (Tomsick et al. 2018; Titarchuk and Seifina 2021), GX 339-4 (Titarchuk and Seifina 2021), Cyg X-3 (Koljonen et al. 2013; Shrader et al. 2010), GRS 1915+105, SS 433 (Sei-

fina & Titarchuk 2010; Titarchuk and Seifina 2021), GS 2000+25, GS 1124-68 and XTE J1550-564 (Zycki et al. 2001) and V4641 Sgr (Titarchuk and Seifina 2021)) in the X-ray spectra in its IS states (for the photon index $\Gamma > 1.9$) under the conditions of zone I (Titarchuk and Seifina 2021; Laurent et al. 2022). However, the question arises as to why HTBB hump is minimal or absent under the conditions of zone II at the same photon indices (Figs. 10 and 11). These results raise a valid question about the nature of the HTBB component as an intrinsic property of a BH.

We found a difference in the spectra from the zone I (enclosed in red) and zone II (enclosed in green in Figure 11) for the same $\Gamma = 2.2 - 2.8$, but for different normalizations N_{com} . Indeed, the HTBB is easier to detect in zone I, while it is barely seen or absent at in

zone II. It is obvious that in zone I the HTBB contribution is well detected, while in zone II the spectrum is well described by the Comptonized model with a minimal HTBB contribution. We demonstrate this difference using the zone I spectra 50128-01-03-00 (left) and 50128-01-02-11 (right) and the zone II spectra 40044-02-01-00 (left) and 40044-02-01-01 (right)). The data are represented by crosses, and the best spectral model `tbabs*(CompTB+BB)` is shown by the red line. The yellow shaded areas show an evolution of the HTBB component during the source transitions between the LHS and the HSS.

Among the possible causes of the formation of the “humps” are the following: 1) Compton reflection, 2) photoelectric absorption of photons below 10 keV in a cold medium (disk), and 3) a gravitationally redshifted AL. Let us consider their possible contribution to the radiation separately.

1) The suggestion that the HTBB hump observed as a positive 20 keV excess in the spectrum is a signature of the Compton reflection (see e.g. [Basko et al. \(1974\)](#); [Sunyaev & Titarchuk \(1980\)](#); [Chakrabarti & Titarchuk \(1995\)](#); [Magdziarz & Zdziarski \(1995\)](#)) faces difficulties given that the hard power-law tails of these spectra are too steep to form a Compton hump. Indeed, [Sunyaev & Titarchuk \(1980\)](#) and later [Laurent & Titarchuk \(2007\)](#) demonstrated that a Compton hump resulting from photon accumulation due to hard photon scattering in a cold medium (e.g. a disk) cannot be obtained if the photon index is $\Gamma > 2$.

2) In principle, the HTBB hump could be a result of photoelectric absorption of photons below 10 keV in the cold medium (disk) given the photoelectric absorption cross-section $\sigma_{ph} \sim (7.8 \text{ keV}/E)^3 \sigma_T$, where E is the photon energy and σ_T is the Thomson cross section (e.g. [Chakrabarti & Titarchuk \(1995\)](#)). [Laming & Titarchuk \(2004\)](#) showed analytically that this reflection hump is not formed if the photon index $\Gamma > 2$.

3) An assumption that the hump of the BH spectrum is caused by a gravitationally redshifted AL is based on the fundamental theoretical conclusions of the General Relativity. It is known that near the event horizon of a BH, conditions arise for the formation of pairs of electrons and positrons with their subsequent annihilation, accompanied by the emission of photons with an energy of 511 keV. This effect is associated with a formation of the AL. In this case, the gravitational field of a BH is so strong that the initial energy of photons, as they move away from the event horizon of a BH, decreases to ~ 20 keV. The line itself is blurred due to the non-zero thickness of the formation layer (for example, ~ 100 m for a BH of a mass of $10 M_\odot$)

and turns into a wide “hump” in the spectrum at 15–40 keV. In fact, [Laurent & Titarchuk \(2018\)](#) showed that photon-photon interactions of efficiently energy-scattered photons lead to powerful pair production near the BH horizon. Indeed, most of the inwardly scattered photons are deflected outward by relativistic free-falling electrons (light aberration effect; see, e.g., [Rybicki & Lightman \(1979\)](#) and Appendix A in [\(Titarchuk and Seifina 2009\)](#)). These outwardly deflected from a BH scattered photons with energy E_{up} interact with the incoming flux photons with energy E_{in} , and this interaction eventually leads to pair production if the condition $E_{up}E_{in} \geq (m_e c^2)^2$ is satisfied. In this case, the converging flow moving with the free-fall velocity v into a BH with the Lorentz factor $\gamma = 1 + z = 1/\sqrt{1 - (v/c)^2} \gg 1$ should reach regions very close to the BH event horizon, $R = R_S + \Delta R \approx R_S(1 + \gamma^{-2})$ ([Titarchuk and Seifina 2009](#)), where $\Delta R = R - R_S$ is the radial distance to the BH horizon. Thus, the created positrons actively interact there with the electrons of the accreting flow, and therefore the photons of the AL are created and distributed in a relatively narrow shell near the BH horizon. In particular, $\Delta R \leq 3 \times 10^4 (10/\gamma)^2 (\mathcal{M}_{BH}/1 M_\odot)$ cm, where \mathcal{M}_{BH} is the BH mass expressed in M_\odot ([Titarchuk and Seifina 2009](#)). Then the proper energy (in the convergent flow to the BH) of the photons of the AL (E_{511}) should be visible to the Earth observer at energies with a redshift of up to

$$E_{511}^{obs} = (1 - R_S/R)^{1/2} E_{511} \approx (\Delta R/R_S)^{1/2} E_{511} \approx E_{511}/\gamma. \quad (14)$$

In result, a significant fraction of these AL photons, strongly gravitationally redshifted, can be directly visible to an observer on Earth as a hump located at ~ 20 keV. For example, for a BH with a mass of $10 M_\odot$, $\Delta R \sim 3 \times 10^4 \times (10/\gamma)^2 \times 10 \sim 100$ m, hence $\gamma = 17$. [Laurent & Titarchuk \(2007\)](#) performed an extensive Monte Carlo simulation of the formation of the X-ray spectrum in a flow converging onto a BH, taking into account photon-electron, photon-photon and pair-electron interactions, which confirms the feasibility of the proposed interpretation in case (3). Indeed, in some cases, the spectra of accreting BHs formed in IS and HSS contain a red-shifted AL located at ~ 20 keV, which can be approximated using the HTBB component.

Interestingly, the NuSTAR spectra of 4U 1957+115 (e.g., *Ns8*) have also been successfully modeled previously, e.g. by [Draghis et al. \(2023\)](#); [Barillier et al. \(2023\)](#) using relativistic X-ray reflection models (`relxill`, `rellxillCp`). We presented here a slightly alternative approach to fitting these data taking into account various physical processes, for which we proposed `compTB` with additional HTBB. We argued that

fits using this model in a wide energy range also lead to good results (right panel of Fig. 9), and also provide motivation for a self-consistent account of these physical processes occurring in 4U 1957+115 during spectral transitions in X-ray outbursts. It is well known that if the photon index Γ is higher than 2, there is no reflection hump (see Laurent & Titarchuk 2007, and also ST80). For example, in Fig. 9 the photon index of the source spectrum is significantly higher than 2, so the observed hump at ~ 20 keV cannot be associated with reflection. Therefore, taking into account the arguments given in (Laurent & Titarchuk 2018), we should accept this hump as due to the formation of an AL near the BH horizon.

5.3. Interpretation of the index saturation and decrease at large \dot{M}

In our study for X-ray observations of 4U 1957+115, we found the correspondence of its X-ray variability with a standard pattern $\Gamma - N_{com}$, typical of accreting BHXRBs during outbursts. Namely, the photon index, Γ increases with normalization N_{com} (which is proportional to \dot{M}) for moderate \dot{M} and saturates at high \dot{M} (zone I in Figs. 10 and 11 (in left red box)). However, after reaching the index saturation phase ($\Gamma \sim 3$) and further increase in normalization N_{com} , Γ drops to values of about $\Gamma = 2$ at even higher \dot{M} (zone II in Figs. 10 and 11 (in right green box)). In fact, we have never seen such a behavior of $\Gamma - \dot{M}$ before (see Fig. 10).

This surprising behavior of Γ versus \dot{M} can be explained by a simple scenario where the innermost accretion region (CC) consists of two layers moving towards the BH, but with different accretion rates. This behavior was predicted by hydrodynamic modeling and its implications for the X-ray observable properties of BHs (Chakrabarti & Titarchuk 1995). They found that one of these flows moved with a very high velocity directly to a BH not forming a shock while another one proceed through the disk and finally forming the shock located within 5–10 Schwarzschild radii from the central object (see Fig. 1 in Chakrabarti & Titarchuk 1995). Because the nature of the flow, there are not enough soft disk photons to illuminate the hot CC. In addition, the Thomson optical depth of the converging flow is quite high, more than $\tau = 3$ and we do not observe the redshifted AL formed near a BH horizon (~ 200 meters from it) at very high accretion rates \dot{M} (Laurent & Titarchuk 2011).

6. CONCLUSIONS

A theoretical idea of the LP formation in a BH relies on the ST85 study. The X-ray LP radiation is a result

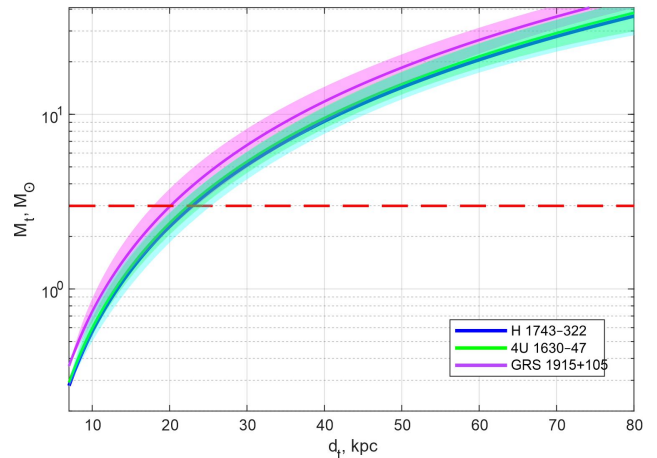


Figure 13. A BH mass m_t versus a distance for a wide range of target source distances given by GAIA’s analysis for 4U 1957+115 (red) using GRS 1915+105 (violet), 4U 1630–47 (blue) and H 1743–322 (green) as the reference sources. The corresponding color bands indicate the areas of $1-\sigma$ estimation errors for each source. Obviously, a BH mass in 4U 1957+115 is more than $5 M_\odot$ (indicated by a red horizontal line) for a source distance greater than 20 kpc.

of the multiple up-scattering of the initially X-ray soft photons environment of the hot CC. Multiple scattering of these soft photons leads to the formation of the emergent Comptonization spectrum. In addition this specific spectrum is linearly polarized if the CC has a flat geometry. The polarization degree of these multiple up-scattered photons P should be independent of the photon energy.

ST85 calculated the radiative transfer of the polarized radiation using the iteration method. A number of these iterations should be much more than average number of scatterings in a given flat CC. As a result, we use the $P - \mu(i)$ diagram, where i is the source inclination. This plot for $P(i)$ in % is calculated for different Thomson optical depths τ_0 of the flat CC from 0.1 to 10 (see also Figs. 5 and 8 in ST85).

Recent IXPE observations revealed the polarization of X-ray radiation of quite a lot of BHXRBs. For the BH source 4U 1957+115, M24 detected a polarization of radiation in HSS at the level of $P \sim 1.9\%$. Given this new information on P and using the $P(i)$ diagram for a given source we estimate the CC optical depth τ_0 . Then, in combination with the results of spectral analysis, we obtain the photon index Γ , the plasma temperature kT_e without any free parameters.

Based on long-term observations of 4U 1957+115 using the *NuSTAR*, *RXTE*, *Suzaku* and *ASCA* observations, we studied its X-ray variability and detected changes in the spectral states during source outbursts. In particular, the existence of two fundamentally differ-

ent types of outbursts was confirmed: soft and hard, which belong to different phases (I and II) of $\Gamma - N_{com}$ correlation. It was shown that the X-ray spectra of 4U 1957+115 are well described by the Comptonization model with the photon index Γ varying from 1.5 to 3. A monotonic increase in Γ with mass accretion rate \dot{M} and saturation of Γ at a level of $\Gamma = 3$ at high values of \dot{M} during X-ray source outbursts were detected. We demonstrated that this behavior of 4U 1957+115, based on a large set of its X-ray observations, is typical of the majority of BHXRBs.

We estimated a BH mass in 4U 1957 using a scaling method $M_{BH} = 4.8 \pm 1.8 M_{\odot}$ assuming the source distance about 20 kpc, based on H 1743-322, 4U 1630-47 and GRS 1915+105 as reference sources. Moreover, a significant transient feature was found in the source spectrum at energies of 10–20 keV, which we attributed to the gravitationally redshifted AL and approximated by the blackbody law with a temperature of 4–5 keV. This feature is observed in the source spectra with the photon index $\Gamma \sim 2.4$ and is presumably formed in a

layer near the BH horizon in 4U 1957+115. We also found a unique phase of the Γ decrease from 3 to 2.4 at very high accretion rates.

ACKNOWLEDGEMENTS

We appreciate valuable remarks by Chris Schrader on the paper. We also recognize the deep understanding of the content of the manuscript by the referee.

Facilities: MAXI, IXPE, NuSTAR, NICER, RXTE, Swift(XRT), Suzaku, ASCA.

Software: HEASoft (HEASARC 2014), XSPEC (Arnaud et al. 1999), CompTB (Farinelli et al. 2008), FTOOLS (Blackburn et al. 1999), ASCASCREEN (Tanaka et al. 1994), *Suzaku* pipeline (Mitsuda et al. 2007), NuSTARDAS (Harrison et al. 2013), IXPEOBSSIM (Baldini et al. 2022).

APPENDIX

A. DATA DESCRIPTION

A.1. *Suzaku* data

Suzaku observed 4U 1957+115 on 2010 May 4 – 17 and November 1. Table 1 summarizes the start and exposure times, and the MJD interval for each of these observations. One can see a description of the *Suzaku* experiment in Mitsuda et al. (2007). For observation obtained by a focal X-ray CCD camera (XIS, X-ray Imaging Spectrometer, Koyama et al. (2007)), which is sensitive over the 0.3–12 keV range, we used software of the *Suzaku* data processing pipeline (ver. 2.2.11.22). We carried out the data reduction and analysis following the standard procedure using the HEASOFT software package and following the *Suzaku* Data Reduction Guide⁴. The spectra of the source were extracted in 0.3–10 keV range using spatial regions within the $4'$ -radius circle centered on the source nominal position (Table 3), while a background was extracted from source-free regions for each XIS module separately. The spectrum data were re-binned to provide at least 20 counts per spectral bin to validate the use of the χ^2 -statistic. We carried out spectral fitting applying XSPEC v12.10.1. The energy ranges around of 1.75 and 2.23 keV are not used for spectral fitting because of the known artificial structures in the XIS spectra around the Si and Au edges. Therefore, for spectral fits we have chosen the 0.3 – 10 keV range for the XISs (excluding 1.75 and 2.23 keV points). In Fig. 2 we show a light evolution curve of 4U 1957+115 whereas green arrows indicate the *Suzaki* observations, listed in Table 1.

A.2. *ASCA* data

ASCA observed 4U 1957+115 on 1994 October 31 – November 1 with total exposure ~ 35 ks (see Table 1, which summarized the start time, exposure time, and the MJD interval). One can see a description of the *ASCA* data by Tanaka et al. (1994). The solid imaging spectrometers (SIS) operated in Faint CCD-2 mode. The *ASCA* data were screened using the standard processing software (ASCASCREEN and FTOOLS) and the standard screening criteria. The spectrum for the source were extracted in 0.3–10 keV range using spatial regions with a diameter of $4'$ (for SISs) and $6'$ (for GISs) centered on the nominal position of the source, while background was extracted from source-free regions of comparable size away from the source. The spectrum data were re-binned to provide at least 20 counts per

⁴ <http://heasarc.gsfc.nasa.gov/docs/suzaku/analysis/>

spectral bin to validate the use of the χ^2 -statistic. The SIS and GIS data were fitted using **XSPEC** in the energy ranges of 0.6 – 10 keV and 0.8 – 10 keV, where the spectral responses are well-known.

A.3. *RXTE* data

We have also analyzed the available data of 4U 1957+115 obtained with *RXTE* (Bradt et al. 1993) (see Table 2). Standard tasks of the LHEASOFT/FTOOLS software package were utilized for data processing using methods recommended by *RXTE* Guest Observer Facility according to the *RXTE* Cook Book⁵. For spectral analysis, we used data from the Proportional Counter Array (PCA) and High-Energy X-Ray Timing Experiment (HEXTE) detectors. *RXTE*/PCA spectra (*Standard 2* mode data, 3 – 50 keV energy range) have been extracted and analyzed using the PCA response calibration (ftool pcarmf v11.1). The relevant deadtime corrections to energy spectra have been applied. In turn, HEXTE data were used for spectral analysis only in the 20–50 keV energy range to exclude channels with the highest uncertainty. We subtracted background corrected in off-source observations. In Figure 4 we present the *RXTE* flux in the 3–50 keV ranges and the observational best-fit spectral characteristics. Here we see that the source experienced three flares (*F1* in 1998, *F2* in 2002 and *F3* in 2005), marked with arrows at the top. Systematic error of 0.5% was applied to the analyzed spectrum.

A.4. *Swift* data

Using *Swift*/XRT data (Evans et al. 2007, 2009) in 0.3–10 keV energy range we studied a total of five observations of 4U 1957+115 during its flaring events from 2007 to 2019 (Table 1). The data used in this paper are public and available through the GSFC public archive. Data were processed using the HEASOFT, the tool **xrtpipeline** and the calibration files (CALDB version 4.1). The ancillary response files were created using **xrtmkarf** v0.6.0 and exposure maps generated by **xrtexpomap** v0.2.7. Source events were accumulated within a circular region with radius of 46" centered at the position of 4U 1957+115 (Table 3). The background was estimated in a nearby source-free circular region of 86" radius. Spectra were re-binned with at least 10 counts in in each energy bin using the **grppha** task in order to apply χ^2 -statistics.

A.5. *IXPE* data

We have also analyzed the available data of 4U 1957+115 obtained with *IXPE* (Weisskopf et al. 2022) at epoch 1, corresponding to the IXPE observation ID=02006601 (*Ix1* in Fig. 2). From cleaned level 2 event data for each gas pixel detector 80" and 60" apertures were used to extract source data in 2–8 keV range for polarimetric and spectroscopic analysis, respectively, using the XSELECT software applying the effective eventnumber weighting (STOKES = "NEFF") to produce products in Stokes *I*, *Q*, and *U* parameters. A background region was extracted from an annulus with inner and outer radii of 132" and 252", centered on the source position (see Table 3). Data were extracted into "polarization cube" structures, allowing ready data slicing by detector, time, energy, etc.

A.6. *NICER* data

NICER observed the source from 12 May, 2023 (MJD 60076) to 23 May, 2023 (MJD 60087), i.e. during the entire IXPE campaign (see Table 1 and Figure 2). Eleven observations during this interval are analyzed covering the rise-peak-decay phase of the outburst. The NICERDAS software is used along with the latest CALDB to reduce the data from the observations. The **nicerl2** task is used to perform standard calibration and screening to generate cleaned event lists. The source and background spectra along with the responses are generated in the 0.5–12 keV energy band using the **nicerl3-spect** task. The spectra are rebinned to have a minimum of 20 counts per energy bin for spectral modelling.

A.7. *NuSTAR* data

We processed *NuSTAR* observations using the **NuSTARDAS** and the latest files available in the *NuSTAR* Calibration Database⁶. We generated clean event files for each observation of 4U 1957+115 using the **nupipeline** task and extracted the source and background spectra in 2–70 keV range from circular regions of 60" and 90" radius, respectively, centered at the source position (Table 3). Source spectra were extracted using the **nuproduct** task. We binned each

⁵ http://heasarc.gsfc.nasa.gov/docs/xte/recipes/cook_book.html

⁶ <http://heasarc.gsfc.nasa.gov/FTP/caldb/data/nustar/fpm/>

spectrum so that there were at least 25 counts per spectral bin. In Figure 2 we indicate using red arrows particular data when 4U 1957+115 was observed by *NuSTAR*.

REFERENCES

- Arnaud, K. A., 1996, in *Astronomical Data Analysis Software and Systems V*, ed. G. H. Jacoby, J. Barnes, Vol. 101, Astronomical Society of the Pacific Conference Series, 17
- Arnaud, K., Dorman, B., & Gordon, C. 1999, XSPEC: An X-ray spectral fitting package, Astrophysics Source Code Library ascl:9910.005
- Baldini, L., Bucciantini, N., Lalla, N. D., et al. 2022 ixpeobssim: Imaging X-ray Polarimetry Explorer simulator and analyzer, Astrophysics Source Code Library, ascl:2210.020
- Barillier, E., Grinberg, V., Horn, D. et al., 2023, ApJ, 944, 165
- Basko, M. M., Sunyaev & Titarchuk, L. G. 1974, A&A , 31, 249
- Bayless, A. J., Robinson, E. L., Mason, P. A., & Robertson, P. 2011, ApJ, 730, 43
- Blackburn, J. K., Shaw, R. A., Payne, H. E., Hayes, J. J. E., HEASARC 1999, FTOOLS: A general package of software to manipulate FITS files, Astrophysics Source Code Library, ascl:9912.002
- Bradt, H. V., Rothschild, R. E. & Swank, J. H. 1993, A&AS, 97, 355
- Chakrabarti, S. & Titarchuk, L. 1995, ApJ, 455, 623 (CT95)
- Chandrasekhar, S. 1950, Radiative transfer, London (Oxford University Press)
- Coppi, P. S., 1992, MNRAS, 258, 657
- Draghis, P. A., Miller, J. M., Zoghbi, A., et al. 2023, ApJ, 946, 19
- Evans, P. A., Beardmore, A. P., Page, K. L., et al. 2009, MNRAS, 397, 1177
- Evans, P.A. et al. 2007, A&A, 469, 379
- Farinelli, R. et al. 2024, A&A, 684, A62
- Farinelli, R., Titarchuk, L., Paizis, A. et al. 2008, ApJ, 680, 602
- Farinelli, R. & Titarchuk, L., 2011, A&A, 525, 102
- Fender, R. P., Garrington, S. T., McKay, D. J., et al. 1999, MNRAS, 304, 865
- Giacconi, R., Murray, S., Gursky, H., et al. 1974, ApJS, 27, 37
- Gaia CollaborationBrown, A. G. A., Vallenari, A., et al. 2021, A&A, 649, A1
- Gaia CollaborationPrusti, T., de Bruijne, J. H. J., et al. 2016, A&A, 595, A1
- Gomez S., Mason P. A., Robinson E. L., 2015, ApJ , 809, L9
- Greiner, J., Cuby, J. G., McCaughrean, M. J. et al. 2001, A&A, 373, L37
- Hakala, P., Muhli, P. and Charles, P., 2014, MNRAS, 4444, 3802
- Harrison, F. A., Craig, W. W., Christensen, F. E. et al. 2013, ApJ, 770, 103
- Ingram, A., Bollemeijer, N., Veledina, A., et al., 2024, ApJ, 968, 76
- Karttunen, H., Kröger, P., Oja, H. et al. 2017, Binary Stars and Stellar Masses. In: Karttunen, H., Kröger, P., Oja, H., Poutanen, M., Donner, K. (eds) Fundamental Astronomy. Springer, Berlin, Heidelberg
- Koljonen, K. I. I., McCollough, M. L., Hannikainen, D. C. & Droulans, R. 2013, MNRAS, 429, 1173
- Koyama, K., Tsunemi, H., Dotani, T. et al. 2007, PASJ, 59, S23
- Kravtsov, V., Berdyugin, A. V., Kosenkov, I. A. et al. 2022, MNRAS, 514, 2479
- Krawczynski, H., Muleri, F., Dovčiak, M., et al. 2022, Science, 378, 650
- Kushwaha, A., Jayasurya, K. M., Agrawal, V. K. et al, 2023, MNRAS, 524, L15
- Kushwaha, A., Jayasurya, K. M., Nandi, A. 2023, arXiv e-prints, p. arXiv:2310.02222
- Laming, M. & Titarchuk, L. 2004, ApJL, 615, L121
- Laurent, P. & Titarchuk, L. 2007, ApJ, 656, 1056
- Laurent, P., & Titarchuk, L. 2011, ApJ, 727, 34
- Laurent, P., & Titarchuk, L. 2018 ApJ, 869, L89
- Laurent, Ph., Titarchuk, L., Seifina, E. 2022, 44th COSPAR Scientific Assembly. Held 16–24 July, 44, 2196
- Maitra, D., Miller, J. M., Reynolds et al. 2014, ApJ, 794, 85
- McClintock, J. E., Remillard, R. A., Rupen, M. P., et al. 2007, arXiv:0705.1034
- Majumder S., Das, S., Agrawal, V. K. et al., 2023, MNRAS, 526, 2086
- Majumder S., Kushwaha A., Das S., Nandi A., 2023, arXiv e-prints, p. arXiv:2309.06845
- Majumder, S., Kushwaha, A., Singh, S., et al., 2025, arXiv e-prints, p. 2506.03774
- McClintock, J., & Remillard, R. 2006, in *Compact Stellar X-ray Sources*, ed. W. H. G. Lewin & M. van der Klis (Cambridge: Cambridge Univ. Press), 157
- Magdziarz, P. & Zdziarski, A. A. 1995, MNRAS, 273, 837

- Matsuoka, M., Kawasaki, K., Ueno, S., et al. 2009, PASJ, 61, 999
- Margon, B., Thorstensen, J. R., & Bowyer, S. 1978, ApJ, 221, 907
- Marra, L., Brigitte, M., Rodriguez Cavero, N. et al. 2024, A&A, 684, 95
- Mitsuda K. et al. 2007, PASJ, 59, S1
- Montanari, E., Titarchuk, L., & Frontera, F. 2009, ApJ, 692, 1597
- NASA High Energy Astrophysics Science Archive Research Center (Heasarc) 2014, HEASoft: Unified Release of FTOOLS and XANADU, Astrophysics Source Code Library, ascl:1408.004
- Nowak M. A., Wilms J., Pottschmidt K. et al. 2012, ApJ, 744, 107
- Nowak M. A., Juett A., Homan J., Yao Y., Wilms J., Schulz N. S., Canizares C. R., 2008, ApJ, 689, 1199
- Nowak, M. A., & Wilms, J. 1999, ApJ, 522, 476
- Ogilvie, G. I., & Dubus, G. 2001, MNRAS, 320, 485
- Orosz J., Kuulkers E., van der Klis M., et al. 2001, ApJ, 555, 489
- Parker, M. L., Buisson, D. J. K., Tomsick, J. A., et al. 2019, MNRAS, 484, 1202
- Podgorný, J., Marra, L., Muleri, F., et al. 2023, MNRAS, 526, 5964
- Ratheesh, A., Dovčiak, M., Krawczynski, H., et al. 2024, ApJ, 964, 77
- Rawat, D., Garg, A., Méndez, M., 2023, ApJ, 949, L43
- Ricci, D., Israel, G. L., & Stella, L. 1995, A&A, 299, 731
- Rodriguez Cavero, N., Marra, L., Krawczynski, H., et al. 2023, ApJ, 958, L8
- Rybicki, G. B. & Lightman, A. P. Radiative processes in astrophysics, A Wiley-Interscience Publication, New York: Wiley, 1979
- Pozdnyakov, L. A., Sobol, I. M. & Syunyaev, R. A. 1983, Astrophys. Space Phys. Res., 2, 189
- Russell, D. M., Lewis, F., Roche, P., et al. 2010, MNRAS, 402, 2671
- Saade, M. L., Kaaret, P., Lioudakis, I. & Ehlert, S. R. 2024, ApJ, 974, 101
- Sanchez-Fernandez, C., et al. 1999, A&A, 348, L9
- Singh, K. P., Apparao, K. M. V., & Kraft, R. P. 1994, ApJ, 421, 753
- Sharma, P., Sharma, R., Jain, C. et al. 2021, RA&A, 21, 214
- Schulz, N. S., Hasinger, G., & Truemper, J. 1989, A&A, 225, 48
- Seifina, E., Titarchuk, L., and Ugolkova, L., 2018a, A&A, 619, 21
- Seifina E., Chekhtman A., Titarchuk L., 2018b, A&A, 613, 48
- Seifina, E., Titarchuk, L., and Virgili, E., 2017, A&A, 607, 38
- Seifina, E., Titarchuk, L., and Shaposhnikov, N., 2014, ApJ, 789, 57
- Seifina, E. & Titarchuk, L. 2010, ApJ, 722, 586
- Shakura, N. I. & Sunyaev R. A. 1973, A&A, 24, 337
- Shaposhnikov, N., & Titarchuk, L. 2009 ApJ, 699, 453
- Sobczak, G. J., McClintock, J. E., Remillard, R. A., & Baleen, C. D. 1999, ApJ, 520, 776
- Sobolev, V. V. 1949, Uchenye Zapisky Leningrad. Univ., Seria, Matem. Nauk, 18, N1163
- Sobolev, V. V. 1966, Astrophysics, 2, 69
- Shrader, C.R., Titarchuk, L. & Shaposhnikov, N., 2010, ApJ, 718, 488
- Steiner, J. F., Nathan, E., Hu, K., et al. 2024, ApJ, 969, L30
- Sunyaev, R. A. & Titarchuk, L. G. 1985, A&A, 143, 374
- Sunyaev, R. A. & Titarchuk, L. G. 1980, A&A, 86, 121
- Sunyaev, R. A. & Truemper, J. 1979, Nature, 279, 506
- Svoboda, J., Dovčiak, M., Steiner, J. F., et al., 2024a, ApJ, 960, 3 (arXiv:2309.10813)
- Svoboda, J., Dovčiak, M., Steiner, J. F., et al., 2024b, ApJ, 966, L35
- Tanaka Y., Inoue H., Holt S. S., 1994, PASJ, 46, L37
- Thorstensen, J. R., 1987, ApJ, 312, 739
- Titarchuk, Mastichiadis & Kylafis 1997, ApJ, 487, 834
- Titarchuk, L. & Zannias, T. 1998, ApJ, 499, 315
- Titarchuk, L. 1994, ApJ, 434, 570
- Titarchuk, L., and Seifina, E., 2009, ApJ, 706, 1463
- Titarchuk, L., Shaposhnikov, N., Seifina, E., 2010, *AIP Conf. Proc.* 1205, 168
- Titarchuk, L., Seifina, E., 2016a A&A, 585, A94
- Titarchuk, L., Seifina, E., 2016b, A&A, 595, 110
- Titarchuk, L., Seifina, E., 2017, A&A, 602, 113
- Titarchuk L., Seifina E., Chekhtman A., Ocampo, I., 2020, A&A, 633, A73
- Titarchuk, L., Seifina, E., 2021, MNRAS, 501, 5659
- Titarchuk, L., Seifina, E., Shrader, Ch., 2023, A&A, 671, A159
- Titarchuk, L., Seifina, E. 2023, A&A, 669, 57
- Titarchuk, L., & Seifina, E. 2024, Front. Astron. Space Sci. 11:1368633
- Titarchuk, L., Seifina, E., Shrader, Ch., 2023, A&A, 671, A159
- Titarchuk, L., Seifina, E., Mishin, E. 2025, A&A, 693, 126
- Titarchuk, L., Soffitta, P. Seifina, E. et al. 2025, A&A, in preparation

- Tomsick, J. A., Parker, M. L., García, Javier A. et al. 2018, ApJ, 855, 3
- Tseovich, V.P. Eclipsing Variable Stars, 1973, New York, J. Wiley
- Yaqoob, T., Ebisawa, K., & Mitsuda, K. 1993, MNRAS, 264, 411
- Veledina, A., Muleri, F., Dovčiak, M., et al. 2023, ApJ, 958, L16
- Weisskopf, M. C., Soffitta, P., Baldini, L., et al. 2022, Journal of Astronomical Telescopes, Instruments, and Systems, 8, 026002
- Wijnands R., Miller J. M., van der Klis M., 2002, MNRAS, 331, 60
- Wilms, J., Allen, A., McCray, R. 2000, ApJ, 542, 914
- White, N. E., & Marshall, F. E. 1984, ApJ, 281, 354
- Zdziarski, A. A., Szanecki, M., Poutanen, et al. 2020, MNRAS, 492, 5234
- Zycki P. T., Done C., Smith D. A. 2001, MNRAS, 326, 1367